Biophysical Journal
Article

Biophysical Society

Mechanotransduction Dynamics at the Cell-Matrix Interface

Seth H. Weinberg,[1] Devin B. Mair,[1] and Christopher A. Lemmon[1,*]
[1]Department of Biomedical Engineering, Virginia Commonwealth University, Richmond, Virginia

ABSTRACT The ability of cells to sense and respond to mechanical cues from the surrounding environment has been implicated as a key regulator of cell differentiation, migration, and proliferation. The extracellular matrix (ECM) is an oft-overlooked component of the interface between cells and their surroundings. Cells assemble soluble ECM proteins into insoluble fibrils with unique mechanical properties that can alter the mechanical cues a cell receives. In this study, we construct a model that predicts the dynamics of cellular traction force generation and subsequent assembly of fibrils of the ECM protein fibronectin (FN). FN fibrils are the primary component in primordial ECM and, as such, FN assembly is a critical component in the cellular mechanical response. The model consists of a network of Hookean springs, each representing an extensible domain within an assembling FN fibril. As actomyosin forces stretch the spring network, simulations predict the resulting traction force and FN fibril formation. The model accurately predicts FN fibril morphometry and demonstrates a mechanism by which FN fibril assembly regulates traction force dynamics in response to mechanical stimuli and varying surrounding substrate stiffness.

INTRODUCTION

Mechanical interactions between cells and their underlying substrate are of great interest and have spawned an entire field of study (reviewed in the literature (1–4)). Previous studies have demonstrated that the elastic modulus of an underlying surface can modulate cell migration (5–8), cell differentiation (9–13), cell spreading (14,15), and cell survival (16–18). Clinical studies have shown that tissue stiffness can have profound effects on disease progression: patients bearing malignant tumors with increased elastic modulus present with more severe disease (19,20); increased elastic modulus in liver tissue is a predictor of cirrhosis (21); and kidney tissue stiffness has been shown to correlate with disease progression in chronic kidney disease (22). Clearly, cells are able to sense the mechanical properties of their surroundings, and subsequent cell fate and function are determined by mechanically transduced signals.

The primary mechanism of mechanotransduction is via transmembrane integrins, which are linked to the actin cytoskeleton via focal adhesion (FA) complexes. Integrins transmit myosin-generated forces that act on the cytoskeleton to the surrounding extracellular substrate. Mechanosensory proteins within the FA complex respond to altered forces and/or strains that result from these interactions, and these forces are altered based on the elastic modulus of the surface to which cells are attached. A previous study from the Odde group elegantly modeled the elements of this system and demonstrated two distinct regimes (23): on rigid surfaces, integrin-substrate rupture events are frequent, so transmitted forces are low (a frictional-slippage regime). On soft surfaces, integrin-substrate rupture events are reduced due to the compliance of the substrate; as such, cells are able to maintain large forces for longer periods of time (a load-and-fail regime). Measured traction forces generated by embryonic chick forebrain neurons support this model (23); however, several experimental studies have indicated contrary data, in which traction forces increase with increasing substrate stiffness (14,24–28).

There are several possible explanations for the variable cellular response to substrate stiffness, including cell-dependent manipulation of actomyosin motor and clutch parameters, as was described in a subsequent study by Bangasser et al. (29). We posit another possible explanation: mechanical modulation by the extracellular matrix (ECM). The ECM is a web of proteins that are assembled by cells; several of the major ECM components are proteins assembled into a fibrillar structure, including collagen, fibronectin, fibrillin, and elastin. These assembled fibrils have unique

Submitted August 25, 2016, and accepted for publication February 21, 2017.

*Correspondence: clemmon@vcu.edu

Editor: Celeste Nelson.
http://dx.doi.org/10.1016/j.bpj.2017.02.027

mechanical properties and serve as intermediate elastic elements between a cell and the substrate to which it is attached. We propose that the cellular response to substrates with varied mechanical properties is mediated by ECM fibrils throughout the assembly process. In this study, we develop a model that accounts for the assembly of one such ECM fibrillar protein in response to cell generated forces, fibronectin (FN).

FN fibrils are one of the earliest ECM proteins assembled during embryogenesis and wound healing (reviewed in Schwarzbauer and DeSimone (30) and Mao and Schwarzbauer (31)). Previous studies have indicated that FN fibrils require actomyosin-based force to assemble (32,33) and are extremely elastic and extensible (34). It is thus reasonable to envision that FN fibril assembly modulates the effective rigidity of an underlying substrate. Previous studies from our group have demonstrated that FN fibrils indeed modify the magnitude of contractile forces generated by cells, regardless of substrate rigidity (14).

We present here a computational model of the actomyosin-FA-FN fibril-substrate unit that simulates the assembly of a single FN fibril and the emergent reciprocal effects of the FN fibril on the effective substrate rigidity and resulting cell-generated contractile force. The model consists of an elastic substrate, represented by a Hookean spring, attached to a series of Hookean springs that represent the extensible domains within a single FN molecule. Integrin binding to FN is represented by a first-order reversible reaction with a force-dependent dissociation rate, and the actomyosin machinery is represented by a pulling force with an inverse force-velocity relationship. When an individual FN domain is stretched beyond a critical threshold, binding of a new FN molecule to the assembling FN fibril is simulated by the addition of a new series of Hookean springs attached in parallel, such that the assembling FN fibril is represented by a large Hookean spring network (Fig. 1). The model accurately reproduces experimental measures of FN fibril morphometry and extensibility. Further, simulations predict

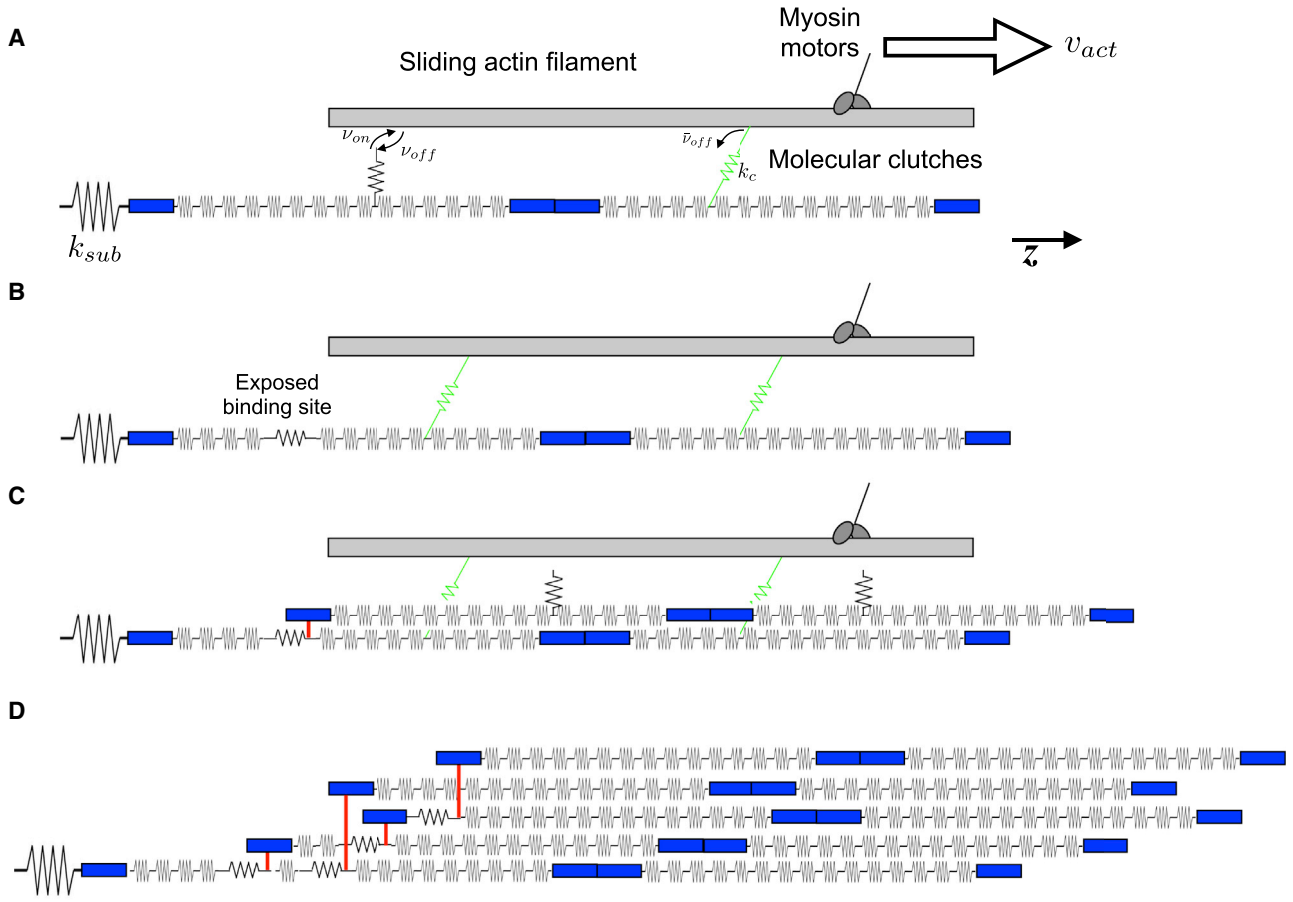

FIGURE 1 Schematic illustration of the FN model. (*A*) Assembly begins with a single FN molecule, represented by 30 springs in series, attached to an elastic substrate, with stiffness k_{sub}. Myosin motors pull on the sliding actin filament at velocity v_{act} along the z axis. Molecular clutches reversibly bind the actin filament with rates v_{on} and v_{off}. Engaged molecular clutches transmit a force proportional to the clutch stiffness k_c, and disengage with a force-dependent off-rate $\bar{v}_{off}$. Note that engaged clutches are connected in parallel with springs representing FN Type III domains. (*B*) Actomyosin-driven forces stretch the FN Type III domains, exposing a cryptic FN binding site. (*C*) A soluble FN molecule in the extracellular space binds to the exposed binding site. (*D*) Subsequent molecular clutch engagement, FN Type III domain stretching, and FN-FN binding events produce an elastic, insoluble FN fibril. To see this figure in color, go online.

that the presence of assembled FN fibrils at the cell-substrate interface creates an intermediate domain between the load-and-fail and frictional-slippage regimes.

MATERIALS AND METHODS

A detailed description of the model formulation, equations, implementation, numerical integration, and parameters is provided in the Supporting Material. An abbreviated model description is given below.

Fibronectin as a series of Hookean springs

Fibronectin consists of a series of nominally 29 independently folded domains. These domains are referred to as Type I, Type II, or Type III, depending on their structure (35,36). While both Type I and Type II domains contain multiple disulfide bonds, which inhibit domain unfolding in response to contractile force, the 15 Type III domains, lacking disulfide bonds, have been shown to unfold in response to contractile force (37–39). Atomic force microscopy experiments have shown that the magnitudes of force required for domain unfolding are unique for many of the domains (39). As such, we model each Type III domain as a time-varying Hookean spring, with a unique resting stiffness, with values determined from experimental data where available (38,39) and estimated based on chemical unfolding data when mechanical data was unavailable (T. Ohashi and H. Erickson, personal communication) (Fig. 1 *A*).

Type I and II domains are present at both the N- and C- terminus of the molecule (nine Type I and two Type II domains at the N-terminus, and three Type I domains at the C-terminus). The lengths of these domains are modeled using available crystal structure data, but because these domains do not unfold, the lengths are merely included as spacing elements with no force-dependent stretch (Fig. 1 *A*, *solid blue regions*). Because FN exists as a homodimer in the extracellular space, each FN molecule is represented by 30 springs in series (one spring per each Type III domain, with 15 Type III domains per FN molecule in each of the two FNs that comprise the dimer) with the requisite lengths added for the nondeformable Type I and II regions at the appropriate locations.

The time-dependent domain spring constant $k_i^j(t)$ and the force $f_i^j(t)$ for the (i,j)th Type III domain are related to the domain node displacements $u_i^j(t)$ and $u_{i+1}^j(t)$ by Hooke's law,

$$f_i^j = k_i^j\left(u_{i+1}^j - u_i^j\right) = k_i^j\epsilon_i^j, \tag{1}$$

where $i \in \{1,\cdots,30\}$, $j \in \{1,\cdots,N_{FN}(t)\}$ are Type III domain and FN molecule indices, respectively; $N_{FN}(t)$ is the total number of FN molecules in the growing FN fibril; u_i^j is the displacement of the (i,j)th Type III domain node from its position equilibrium in the absence of force; and $\epsilon_i^j = u_{i+1}^j - u_i^j$ is the elongation or stretch of each Type III domain. The time-dependency of the domain spring constant, $k_i^j(t)$, is described in Modeling Nonlinear Stiffness of FN Domains, below.

The elasticity of the substrate is represented by a Hookean spring, with spring constant k_{sub}, connected in series with the spring representing FNIII-1 of the first FN molecule at one node (Fig. 1 *A*). The other node of the substrate spring is fixed, i.e., the displacement equal to 0 is an imposed relationship, or boundary condition. Thus, the elongation or stretch of the substrate is $\epsilon_{\text{sub}} = u_1^1$, the node displacement for the first domain in the first FN molecule.

Modeling cell-FN binding

Cells bind to FN via transmembrane integrins, specifically binding to an arginine-glycine-asparagine loop in the 10th Type III domain of FN (40). Following the approach by Chan and Odde (23), we represent the cell-FN connection with a single Hookean spring with spring constant k_c and refer to this connection as a "molecular clutch" (Fig. 1 *A*, *green springs*). When engaged, clutch springs are connected in parallel with the springs representing FN Type III domains. In our model, integrin binding to the FNIII-10 domain, i.e., clutch engagement/disengagement, is represented as a stochastic first-order reversible reaction,

$$\text{(disengaged) } \mathcal{D} \underset{\overline{\nu}_{m,\text{off}}^j}{\overset{\nu_{\text{on}}}{\rightleftharpoons}} \mathcal{E} \text{ (engaged)}, \tag{2}$$

where ν_{on} and $\overline{\nu}_{m,\text{off}}^j$ are rates with units of inverse time; and $m \in \{1,2\}$ is the index of the clutch. Engaged clutches build tension, as the connection via the clutch spring is stretched by actin motion.

Increased traction forces increase the likelihood of rupture events between integrins and the FNIII-10 domain, represented by modeling the dissociation rate as force-dependent according to Bell's Law (41),

$$\overline{\nu}_{m,\text{off}}^j = \nu_{\text{off}}\exp\left(f_{c,m}^j \Big/ f_b\right), \tag{3}$$

where ν_{off} is the disengagement rate in the absence of clutch displacement; f_b is a break force; and the clutch force $f_{c,m}^j(t)$ in the (m,j)th clutch is given by

$$f_{c,m}^j = k_c\left(u_{c,m}^j - u_{10m+1}^j\right), \tag{4}$$

and $u_{c,m}^j(t)$ is the displacement of the (m,j)th clutch node from its equilibrium position. The displacement $u_{10m+1}^j(t)$ represents the displacement of the two FNIII-10 domains in the jth FN dimer, with indices 11 and 21, respectively.

Modeling actomyosin force transmission to FN

Actomyosin force transmission is modeled as in the Chan-Odde model (23). Integrins, acting as a molecular clutch, transmit actomyosin forces to the assembling FN fibril. The interaction between actin velocity and transmitted myosin force is governed by an inverse force-velocity relationship that was described in Chan and Odde (23) and Bangasser et al. (29) and which is supported by retrograde actin velocity experiments (42,43),

$$v_{\text{act}} = v_u\left(1 - \frac{f_{\text{sub}}}{f_{\text{stall}}}\right), \tag{5}$$

where v_{act} is the actin velocity; v_u is the unloaded actin velocity; f_{stall} is a stall force dependent on the number of myosin motors; and traction force is $f_{\text{sub}} = k_{\text{sub}}\epsilon_{\text{sub}}$.

The extension of FNIII-10-bound integrins is calculated from the actin filament velocity (Fig. 1), producing deflections of each individual domain in the assembling FN fibril, such that, assuming a rapid equilibrium, node positions for each domain can be solved by the direct stiffness method, a standard finite element method approach (44). The resulting traction force f_{sub}, in turn, feeds back on the actin filament velocity. When traction force reaches the stall force, actin filament velocity is zero and assembly terminates.

Modeling FN-FN interactions in an assembling fibril

Previous studies have indicated that FN fibrils only assemble when FN molecules are subjected to cell contractile forces (32,33), and have suggested that there is a buried cryptic binding site in FN molecules that only is exposed when under tension (32). Based on prior work (45), we assign a threshold value for domain stretch ϵ_t, above which the domain is likely to be able to bind to a soluble FN molecule. FN binding is modeled as a

two-step process: binding site exposure, followed by soluble FN binding to the exposed binding site. Binding site exposure is modeled as a stochastic process, with probability π_i^j predicted by a Hill equation with a half-maximal response when domain stretch is equal to ϵ_t,

$$\pi_i^j = \frac{\left(\epsilon_i^j\right)^\eta}{\left(\epsilon_i^j\right)^\eta + \epsilon_t^\eta}, \tag{6}$$

where η is a scaling factor that determines the threshold steepness. Soluble FN can then bind to an exposed binding site via a stochastic irreversible reaction.

Which domains contain the cryptic FN-FN binding sites? Deletion mutant studies in which each Type III domain of FN is serially deleted have demonstrated that no Type III domain is absolutely required, with the exception of the 10th Type III domain, the site of integrin attachment (46). This suggests that there are multiple FN-FN binding sites. We have previously hypothesized that all 15 Type III domains are capable of facilitating FN-FN binding (14). This is notably only one possible hypothesis for FN assembly at the molecular level. For this study, we utilize this mechanism; however, the model has been formulated to test alternative hypotheses with a smaller subset of FN-FN binding sites. Future studies will explore the effects of specific FN binding locations on the geometry and extensibility of FN fibrils.

Modeling the three-dimensional architecture of the FN fibril

The model simulates FN fibril assembly and extension along a single dimension (i.e., the z axis). While individual domain stretch is directed along the z axis, the model additionally accounts for the three-dimensional (3D) architecture of the assembling FN fibril by defining the location of each FN molecule in the x,y plane, to compare simulation results to experimental measures of FN fibril morphometry. While there is no data indicating the 3D FN fibril architecture, there are likely steric hindrances that limit the addition of new FN molecules to the assembling fibril. As such, we model the growing fibril using a hexagonal packing geometry (Fig. 2 *B*). Each FN molecule can have at most six neighbors in the x,y plane. When a soluble FN molecule binds to an exposed binding site, the new FN molecule is assigned randomly to an open position around the stretched FN molecule. Once all six positions are occupied, a FN molecule is considered interior and is incapable of binding additional FN molecules. Additionally, integrin attachment (described above) is limited to FNIII-10 domains on perimeter FN molecules; interior FN molecules are considered to be sterically hindered from attaching to the cell surface.

Modeling nonlinear stiffness of FN domains

Each Type III domain is modeled as a Hookean spring, such that the spring force is proportional to the elongation of the spring. However, it is not physiologically accurate to represent each domain as a spring with a constant stiffness, because both experimental and computational studies suggest that the domain stiffness changes as the domain unfolds (39,45,47). While previous studies have demonstrated that Type III domains have unique mechanical unfolding properties (39), we assume that these unique properties only exist until secondary structures are disrupted, after which point, domains are modeled as unstructured polypeptides that behave as entropic springs. Stiffness in this regime can be modeled using the wormlike chain (WLC) model (48,49). The WLC model relates the extension and force of a semiflexible polymer that, importantly, accounts for the nonlinearity in the force-extension relationship as the polymer approaches its full contour length. To account for both the domain-specific mechanical properties when domains are folded, and the domain-independent, WLC behavior at larger stretches, we formulated a stretch-dependent stiffness relationship in which the stiffness at rest is determined from published data, and approaches an identical WLC-predicted stiffness as stretch increases (Fig. 3):

The steady-state stretch-dependent domain stiffness $k_i^\infty(\epsilon_i^j)$ transitions between the regimes for unique stiffness and the identical WLC-governed stiffness, i.e., $k_i^\infty(0) = k_{i,0}$ (see Table S2), and for large ϵ_i^j, k_i^∞ approaches $k_\omega(\epsilon_i^j)$,

$$k_i^\infty\left(\epsilon_i^j\right) = k_\omega\left(\epsilon_i^j\right) + [k_{i,0} - k_\omega(0)]\exp\left(-\epsilon_i^j/\lambda_\omega\right), \tag{7}$$

where λ_ω is a length scale that defines the regime transition; and k_ω is defined below. For large domain stretches, the WLC model relates the molecular force F_ω and stretch or elongation ϵ,

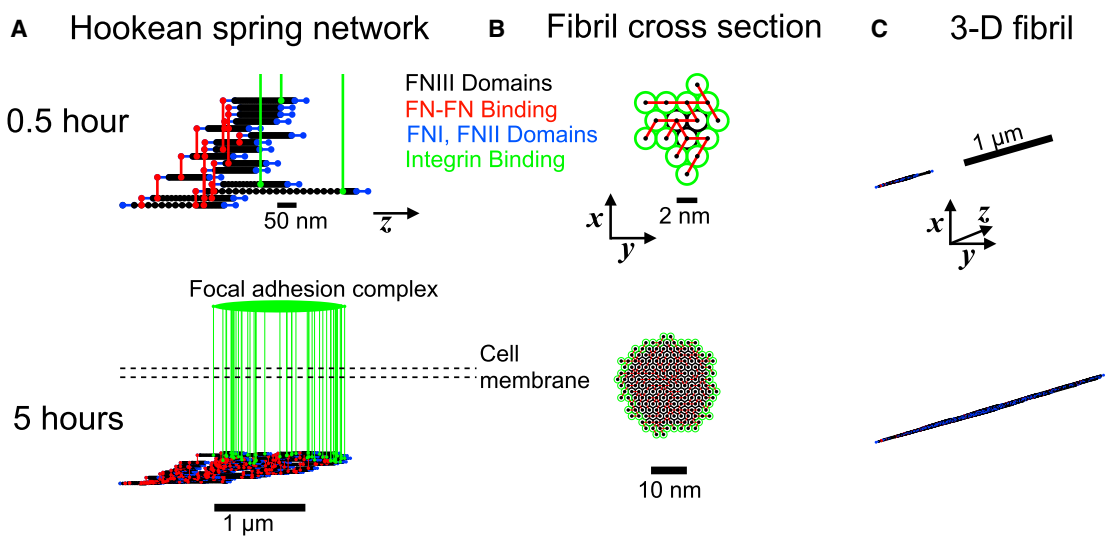

FIGURE 2 Structure and architecture of the assembling fibronectin fibril. A representative simulation structure and architecture are shown at 0.5 and 5 h. (*A*) The Hookean spring network connections along the z axis are shown: elastic FN Type III domains (*black*), FN-FN binding (*red*), inelastic FN Type I and II domains (*blue*), and integrin binding (*green*) are shown. The FA complex is illustrated in the intracellular space as spanning the range of FN-bound integrins. (*B*) The FN fibril cross section in the x,y plane is shown, with FN-FN connections (*red*). Interior and exterior FN molecules are shown in black and green, respectively. (*C*) The 3D FN fibril architecture is shown. Parameters: $k_{sub} = 1000$ pN/nm. To see this figure in color, go online.

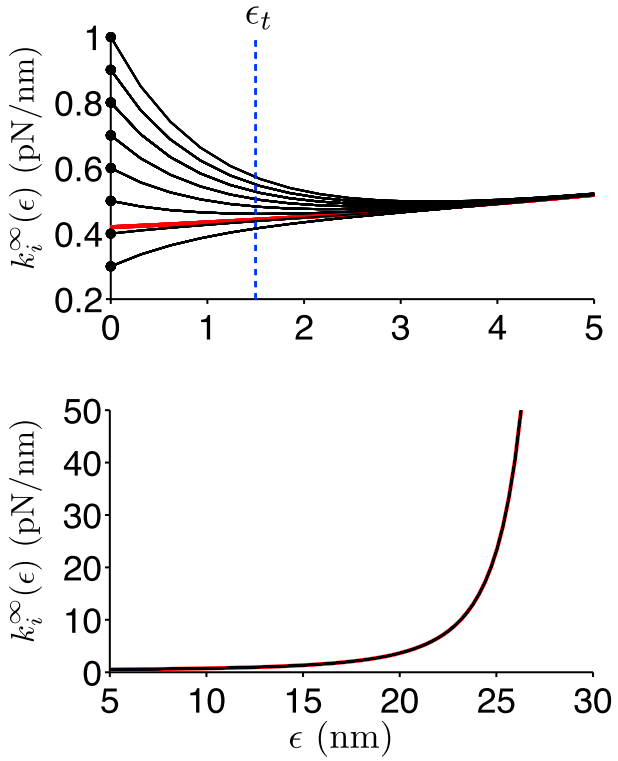

FIGURE 3 Nonlinear spring stiffness for FN Type III domains. The steady-state spring stiffness values for the FN Type III domains (k_i^∞ in Eq. 7) are shown as a function of the domain stretch ϵ. (*Top*) In the absence of actomyosin forces and small domain stretch, each FN Type III domain spring constant k is equal to a unique spring constant $k_{i,0}$ (Table S2), representing the unique mechanical properties of each FN Type III domain (*black lines*). (*Bottom*) In the presence of large actomyosin forces and large domain stretch, domain stiffness values are governed by a WLC model, producing a highly nonlinear increase in domain stiffness. (*Red line*) Domain binding site exposure threshold ϵ_t. (*Dashed vertical blue line, top panel*) To see this figure in color, go online.

$$F_\omega(\epsilon) = \left(\frac{k_B T}{\chi_p}\right)\left[\frac{1}{4(1-\epsilon/\chi_d)^2} - \frac{1}{4} + \frac{\epsilon}{\chi_d}\right], \qquad (8)$$

where k_B is the Boltzmann's constant; T is the absolute temperature; χ_p is the domain persistence length; and χ_d is the domain contour length. To relate the WLC model to the spring network that is the basis of our model, we define the spring constant k_ω relating the force F_ω and displacement ϵ of spring from rest as the derivative of F_ω in Eq. 8, respective to ϵ,

$$k_\omega(\epsilon) = \frac{dF_\omega}{d\epsilon} = \left(\frac{k_B T}{\chi_d \chi_p}\right)\left[\frac{1}{2(1-\epsilon/\chi_d)^3} + 1\right]. \qquad (9)$$

Accounting for the dynamics of the transition between domain stiffness regimes, the time-varying domain stiffness $k_i^j(t)$ is governed by a first-order isomerization reaction, with steady-state domain stiffness $k_i^\infty(\epsilon_i^j)$ (Eq. 7) and time constant τ_ω,

$$\frac{dk_i^j}{dt} = \frac{k_i^\infty(\epsilon_i^j) - k_i^j}{\tau_\omega}. \qquad (10)$$

Our approach allows us to define stretch- and time-dependent stiffness relationships, for which we can define unique mechanical properties at rest and characteristic polymer entropic spring properties, including domain persistence and contour length, in the WLC regime, using simple first-order differential equations, without necessitating a significantly more complex system based on viscoelastic materials, e.g., the Maxwell or Kelvin-Voigt models.

FN fibrils assembly simulations

Simulation of FN fibril assembly involves timescales ranging over several orders of magnitude: Molecular clutch engagement/disengagements are stochastic events occurring on the order of milliseconds, while FN fibril assembly occurs on the order of hours to days. To simulate fibril assembly, we utilize a multiscale hybrid stochastic-deterministic integration scheme that enables the use of a relatively large numerical integration time step, while still appropriately accounting for clutch engagement/disengagement stochastic events. Details are provided in the Supporting Material.

Simulations were performed in the software MATLAB (The MathWorks, Natick, MA). Computational time mean ± SD was 66.8 ± 32.7 h using high performance computing nodes with Xeon E5-2670 2.5-GHz v2 processors (Intel, Santa Clara, CA). Summary measurements (see Figs. 5, 6, and 7) are averaged over the final 10 min of simulation time, to account for measurement fluctuations arising due to integrin binding and unbinding events (k_{sub} = 1000 pN/nm, 500 simulations; all other k_{sub} values, 100 simulations).

Experimental quantification of FN fibril geometry

To quantify FN fibril morphometry, 10^5 WI-38 human embryonic lung fibroblasts (American Type Culture Collection, Manassas, VA) were plated on 12-mm-diameter glass coverslips coated in 40 nM FN. Cells were allowed to assemble fibrils and were fixed at determined intervals ranging from 3 to 72 h. After fixing, cells were immunofluorescently labeled using a polyclonal FN antibody. After acquisition of immunofluorescence images, the properties of individual FN fibrils were analyzed with custom MATLAB code using the image processing toolbox, to quantify individual FN fibril area, length, and total fibril count per image. Each experiment was repeated in triplicate for each time point. Data was acquired for 20 images from each experimental replicate.

To collect FN force measurements, cell-generated traction forces were quantified as previously described in Scott et al. (14). Briefly, 40,000 cells were plated on microfabricated post array detectors (mPADs). Post deflection was measured based on the positions of the tops and bottoms of the posts. For a given deflection, beam bending theory was utilized to calculate force, based on post height, the elastic modulus, and the moment of inertia. Each experiment was repeated in triplicate for each time point. Data was acquired for 20 cells from each experimental replicate.

RESULTS

Model predicts FN fibrils with physiologically accurate architecture, extensibility, and traction forces

Numerical simulations of our model were performed for 30 h of simulation time, or until assembly termination via stalled actin filaments. Spring network architecture and fibril geometry is shown for a representative simulation in Fig. 2. Hookean spring connections are shown among Type III domains (*black*), connected FN molecules (*red*),

and bound integrins (*green*), in addition to inelastic Type I and II domains (*blue*) (Fig. 2 *A*). While the FA complex is not explicitly represented in simulations, model predictions of the FA complex length can be made based on measures of the length between the most proximal and distal FN-bound integrin connections (*green oval*). The fibril cross section illustrates the hexagonal packing structure of individual FN molecules (Fig. 2 *B*), and a 3D view illustrates the size of the assembling FN fibril, with all axes on the same scale (Fig. 2 *C*). Movie S1 shows the FN fibril spring network and geometry throughout assembly.

Time-series measurements from the same simulation are shown in Fig. 4. The number of FN molecules per fibril increases approximately linearly with time (Fig. 4 *A*). Fibril length is represented by two measurements: the stretched length, which represents the total length of the fibril while under tension from the actomyosin-induced forces (Fig. 4 *B*); and the relaxed length, in which tension is removed (Fig. 4 *C*). The relaxed length is determined solely based on the Hookean spring network architecture (Fig. 2), assuming that all spring nodes are in their respective equilibrium position. Both stretched and relaxed length increase as a function of time and approach a steady-state value, as does fibril thickness (Fig. 4 *D*), which is measured as the maximum diameter of fibril cross section.

Our model predicts that FN fibril extensibility, given by the stretched-relaxed length ratio, approaches a value of ~4 (Fig. 4 *E*), in close agreement with previous experimental measures of a maximum of fourfold extensibility in cell-derived FN fibrils (34). Force on the fibril increases as a function of time, (Fig. 4 *F*), consistent with our prior work (14,33). In concert with the increase in substrate force, actin velocity decreases while the fraction of attached molecular clutches increases as a function of time. (Fig. 4, *G* and *H*). FA length is predicted to gradually increase, following a similar time course as stretched and relaxed FN length and substrate force (Fig. 4 *I*).

Histograms of terminal FN fibril measurements are shown for a population of 500 simulations in Fig. 5. To account for stochasticity, measurements were averaged over the final 10 min preceding assembly termination for each simulation. In general, the distributions for FN fibril sizes (FN molecule, stretched and relaxed length, and thickness) were left-tailed, i.e., the population mean (*red dashed line*) is less than the distribution peak (Fig. 5, *A–D*). Thus, while most FN fibrils exhibited significant assembly, as in the example in Fig. 4, the model also predicts a small population of smaller FN fibrils. Most FN fibrils exhibited extensibility between 2.5 and 4.5 (Fig. 5 *E*). Just preceding assembly termination, substrate force typically approached the stall force (200 pN), such that actin velocity was typically near zero (Fig. 5, *F* and *G*). The distribution of the fraction of attached molecular clutches was also left-tailed, with the largest number of FN fibrils exhibiting greater than half of clutches attached at assembly termination (Fig. 5 *H*). The predicted FA length distribution was symmetric, with an average of 2.5 μm, with most FA complexes between 1 and 4 μm (Fig. 5 *I*). The average FN assembly time was ~14.5 h; however, the distribution of FN assembly time was bimodal, with a small peak at 4 h corresponding to small fibrils and a larger peak at 16 h corresponding with larger fibrils (Fig. 5 *J*). Interestingly, all FN fibril size measurements are highly correlated with FN assembly time (Pearson correlation coefficient, 95% confidence interval: FN molecules 0.949 (0.940,0.957); stretched length 0.769 (0.730,0.802);

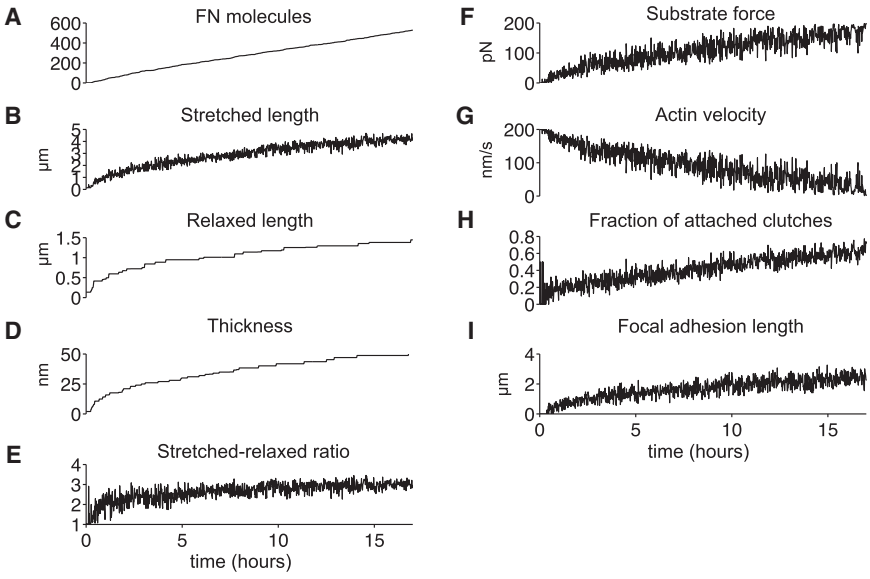

FIGURE 4 Morphometrical, mechanical, and biochemical properties during FN fibril assembly. (*A*) The number of FN molecules, (*B*) stretched length, (*C*) relaxed length, (*D*) thickness, (*E*) extensibility, given by the stretched-relaxed length ratio, (*F*) substrate force, (*G*) actin filament velocity, (*H*) the fraction of attached molecular clutches, and (*I*) the FA length are shown as a function of time for a 16-h simulation of an assembling FN fibril. The fraction of attached molecular clutches is given by total clutches bound to the FN Type III-10 domain, divided by the total number of clutches available for binding (two per exterior FN molecule). Measurements are for the simulation presented in Fig. 2.

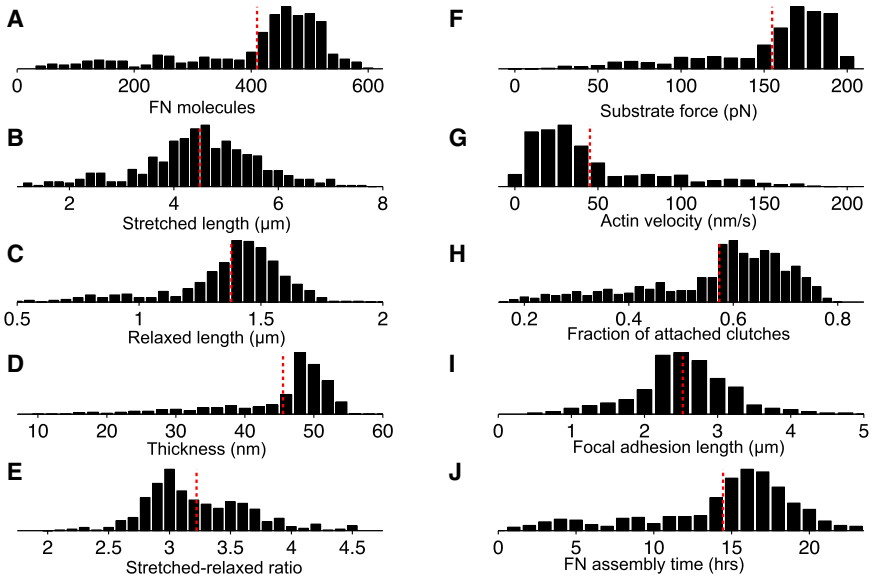

FIGURE 5 Summary of morphometrical, mechanical, and biochemical properties of assembled FN fibrils. Histograms for the following measurements and properties are shown for 500 numerical simulations: (*A*) number of FN molecules, (*B*) stretched length, (*C*) relaxed length, (*D*) thickness, (*E*) extensibility, given by the stretched-relaxed length ratio, (*F*) substrate force, (*G*) actin filament velocity, (*H*) the fraction of attached molecular clutches, and (*I*) FA length. (*J*) Summary data for total assembly time is shown. In all panels, the dashed red line denotes the mean. Parameters: $k_{sub} = 1000$ pN/nm. To see this figure in color, go online.

relaxed length 0.838 (0.810,0.862); thickness 0.920 (0.905,0.932); all $p < 10^{-10}$).

FA length and FN fibril morphometrical and mechanical properties are related in a substrate stiffness-dependent manner

The model predicts a similar time course between the FA length and assembled FN fibril morphometrical and mechanical properties (Fig. 4). Further, our model predicts that substrate force, and relaxed and stretched length of the assembled FN fibril are positively correlated with the FA length, independent of substrate stiffness (Fig. 6), consistent with our previously shown experimental results (14).

We next investigated the substrate stiffness dependency of the relationship between FA length and fibril properties. The substrate force-FA length ratio, or FA stress, is predicted to have a U-shaped dependence on substrate stiffness (Fig. 6 *A*), consistent with 2010 experiments from the Chen lab, showing FA stress increasing with substrate stiffness for more rigid substrates (25).

The relaxed FN fibril length-FA length ratio ranges from ~0.5 to 0.6 and also generally follows a U-shaped dependence on substrate stiffness (Fig. 6 *B*), while the stretched FN fibril length-FA length ratio ranges from ~1.6 to 1.9 and generally increases on more rigid substrates (Fig. 6 *C*). Thus, the model predicts that, on average, FA length is approximately twice the relaxed fibril length, while approximately half of the stretched fibril length, with moderate substrate stiffness dependence. Finally, the positive correlation between fibril extensibility and FA length demonstrates that longer FAs are associated with greater fibril elasticity (Fig. 6 *D*). The extensibility-FA length ratio ranges from ~0.2 to 0.5 and generally increases on more rigid substrates.

FN fibrils create an intermediate regime between frictional slippage and load-and-fail and are only weakly dependent on substrate modulus

Next, we investigated the dependence of substrate stiffness in our model, and compared with the Chan-Odde model, to demonstrate the importance of FN fibril interactions with the cell and substrate (Fig. 7). As was previously observed (23), the Chan-Odde model predicts large substrate deflections and large forces on soft surfaces (*black lines*) that precipitate periodic catastrophic integrin-substrate rupture events (i.e., load-and-fail regime), resulting in a rapid decrease to zero traction forces, while near-zero deflections and small forces are observed on stiff surfaces (*red lines*), due to frequent rupture events (i.e., frictional-slippage regime) (Fig. 7 *A*).

Interestingly, our model predicts an intermediate regime that does not strictly follow the dynamics of either of the two extreme load-and-fail or frictional-slippage regimes, because, critically, rupture event occurrences are intermediate to both the catastrophic and the frequent rupture events observed in the Chan-Odde model for soft and rigid substrates, respectively (Fig. 7 *B*). On soft surfaces, our model predicts that the maximum substrate deflection and forces are smaller, compared with the Chan-Odde model, while the minimum deflection and forces do not approach zero (*black lines*). On rigid surfaces, substrate deflection is still small, but also nonzero, while traction forces are much larger, compared with the Chan-Odde model (*red lines*). As a result of this intermediate regime, overall, substrate forces are similar for both soft and rigid substrates.

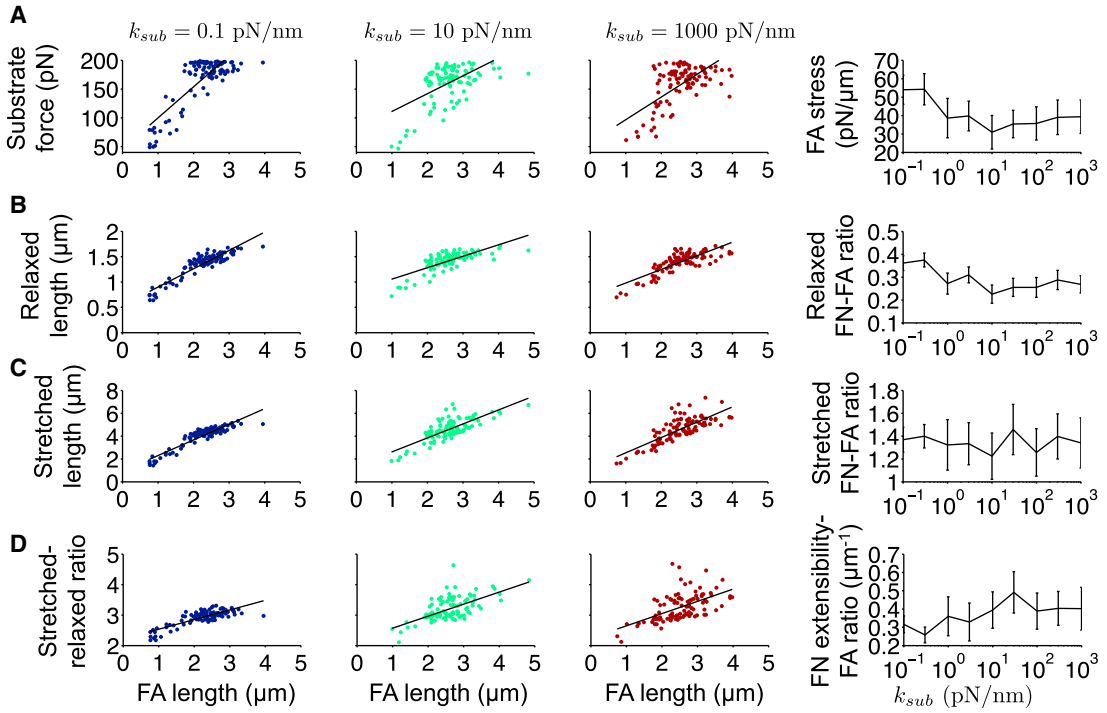

FIGURE 6 Model predictions for the relationship between FA length and assembled FN fibril morphometrical and mechanical properties. (*Left three panels*) (*A*) Substrate force, (*B*) relaxed FN fibril length, (*C*) stretched FN fibril length, and (*D*) fibril extensibility (stretched-relaxed FN length ratio) are plotted as a function of predicted FA length, for different values of substrate stiffness k_{sub}. Each dot represents a single simulation. (*Right panels*) (*A*) FA stress (substrate force-FA length ratio), (*B*) relaxed FN length-FA length ratio, (*C*) stretched FN length-FA length ratio, and (*D*) FN extensibility-FA length ratio, as determined by a linear least squares fit, are shown as a function of k_{sub}. To see this figure in color, go online.

Physiologically, this suggests that FN fibrils may serve to compensate for detrimental effects of either soft or rigid substrates by inserting an elastic fibril between cell and substrate.

The critical difference between the models can be summarized as follows: In the Chan-Odde model, both traction forces and integrin-substrate binding dynamics evolve at a single location—the cell-substrate interface. However, in our model, traction forces and integrin-fibril binding are distributed throughout the highly elastic assembling fibril, which mitigates both catastrophic and frequent rupture events. As such, the presence of the assembling fibril in our model facilitates, on average, much larger traction forces (Fig. 7 *C*), due to an increased likelihood of attached molecular clutches, i.e., integrin binding (Fig. 7 *D*), compared with the Chan-Odde model, for all substrate stiffness values. This is in agreement with a previous study from our group, in which we demonstrated that the presence of FN fibrils was necessary for WI-38 lung embryonic fibroblasts to generate large forces on rigid substrates (14).

Simulation outputs indicate that the degree of FN assembly and the morphology of FN fibrils is similar across a range of physiologically relevant stiffness values (Fig. 7, *E–H*), in agreement with previously published work from our lab that indicates similar degrees of FN fibril assembly regardless of substrate stiffness (14). Only the stretched-relaxed length ratio and, to a lesser extent, the stretched length show a significant correlation with substrate stiffness.

Further model analysis of fibril morphometric and mechanical properties and substrate stiffness is provided in the Supporting Material, detailing the role of both fibril architecture and Type III domain extension on fibril length and the U-shaped dependence of FA stress on substrate stiffness (Fig. S1). Our model also predicts that increasing unloaded actin velocity (v_u; see Eq. 5) greatly truncates the fibril assembly process, due to frequent integrin binding rupture events comparable to frictional-slippage dynamics (Fig. S2).

Experiments and simulations predict stable FN fibril size

To evaluate the efficacy of the model, we quantified FN fibril morphometry and forces as a function of time in WI-38 human lung embryonic fibroblasts, cells representative of a stereotypical fibroblast morphology (50). Representative images of FN fibrils are shown at 3, 12, and 24 (Fig. 8 *A*), with custom image processing identifying individual fibrils and quantifying fibril length (Fig. 8 *B*). A representative composite image of a cell and mPADs is shown, used to measure cell-generated forces (Fig. 8 *C*).

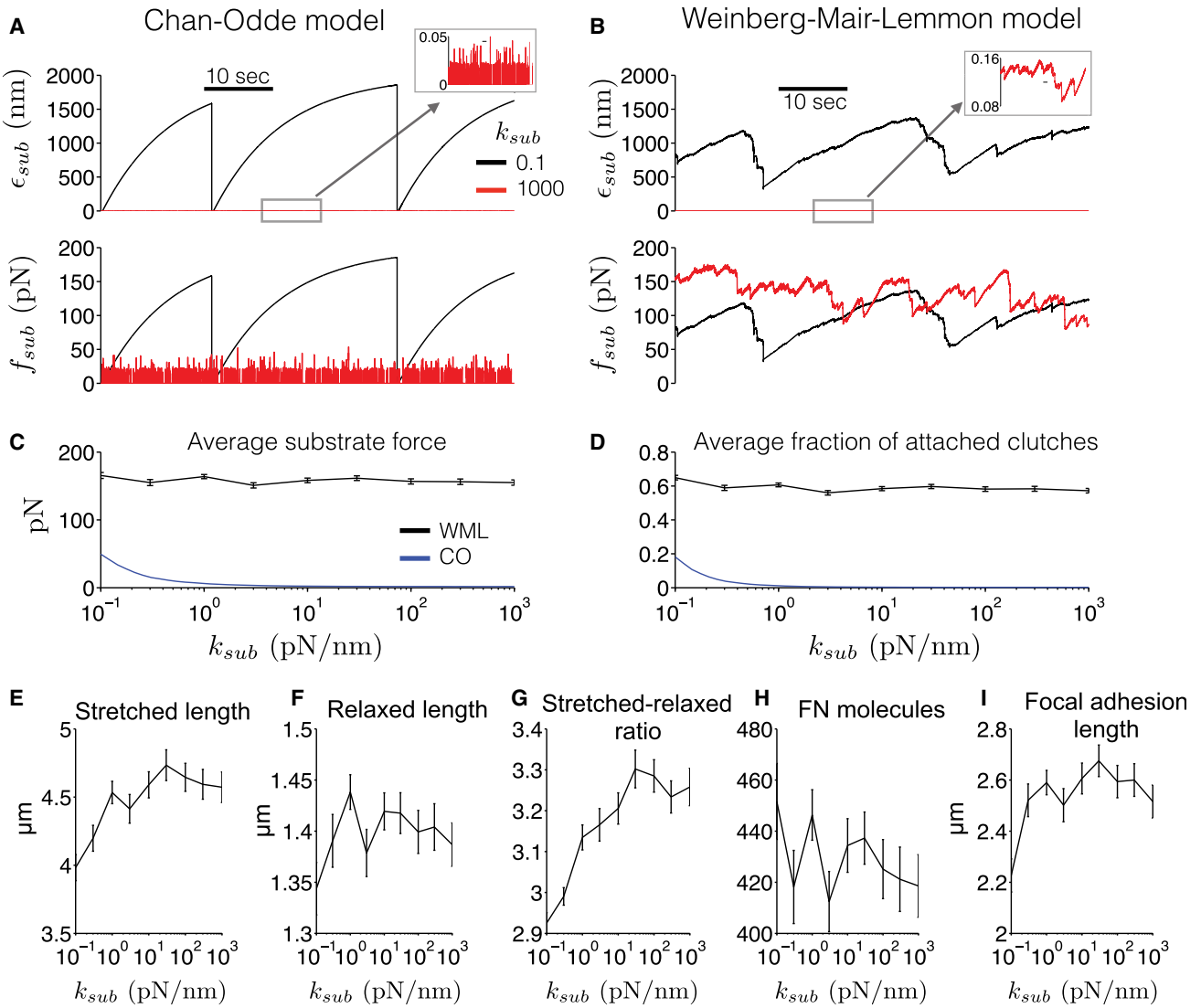

FIGURE 7 Mechanotransduction model predictions of substrate stiffness dependence. (*A*) Chan-Odde (CO) model is simulated (23), using model parameters given in Tables S1 and S2. Substrate deflection ϵ_{sub} (*top*) and force f_{sub} (*bottom*) are shown as a function of time on soft (*black lines*) and rigid (*red lines*) substrates, illustrating the load-and-fail and frictional-slippage regimes, respectively. (*B*) Substrate deflection and force, from simulations of our model (Weinberg-Mair-Lemmon, WML), illustrate an intermediate mechanotransduction regime. WML model mean ± SE, for (*C*) substrate force and (*D*) fraction of attached molecular clutches are shown as a function of substrate stiffness k_{sub} in the CO (*blue lines*) and WML (*black lines*) models. Mean ± SE, for (*E*) stretched length, (*F*) relaxed length, (*G*) stretched-relaxed length ratio, (*H*) number of FN molecules, and (*I*) FA length are shown as a function of k_{sub}. Pearson correlation coefficient between the logarithm of k_{sub} and WML model means (95% confidence interval): (*E*) 0.779 (0.237,0.951), $p = 0.013$, (*F*) 0.290 (−0.463,0.800), $p = 0.445$, (*G*) 0.871 (0.490, 0.973), $p = 0.0022$, (*H*) −0.467 (−0.863, 0.286), $p = 0.205$, (*I*) 0.557 (−0.169, 0.8915), $p = 0.119$. In (*C*) and (*D*), CO model means are computed by time-averaging over a 1-min simulation. In (*C*)–(*I*), WML model averages are computed by time-averaging over the minute preceding FN assembly termination, and then averaged over 100 simulations. To see this figure in color, go online.

Summary analysis shows that individual FN fibril length increases as a function of time, with fibrils reaching steady-state values at ~18 h, comparable to the duration of FN assembly predicted by the model (Fig. 8 *D*). Importantly, model predictions of FN fibril length, as both a function of time and at a steady state, closely match experimental measurements, with some deviation at early time points when fibril counts are low. We next measured the time-dependence of traction forces to compare with the model, normalizing force values due to in vitro FN fibrils often spanning multiple posts, distributing forces and thus reducing force magnitude. Importantly, simulations accurately reproduce the time-dependent increase in cell-generated traction force, also reaching a steady state at ~18 h (Fig. 8 *E*).

DISCUSSION

Previous models of cell-substrate mechanical interactions fail to account for the extracellular matrix, an intermediate

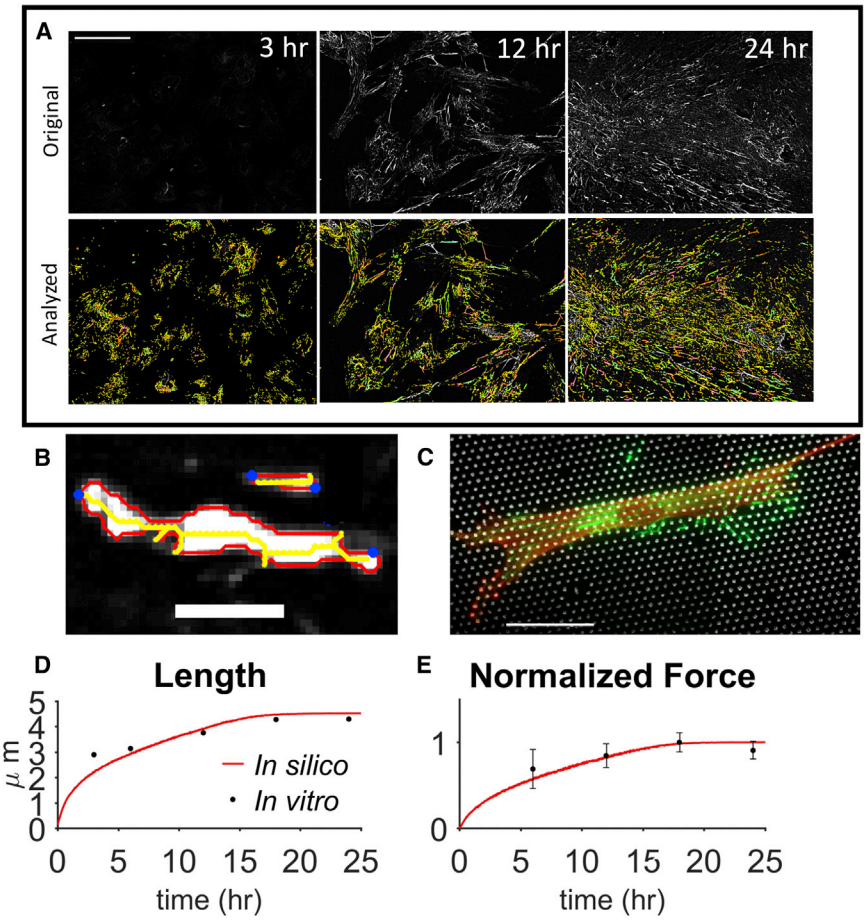

FIGURE 8 FN fibril in vitro morphometrical and force measurements. (*A*) Raw (*top*) and analyzed (*bottom*) FN fibril images at different time points. Scale bars, 100 μm. (*B*) Two analyzed FN fibrils, in which custom image processing measures fibril image outline (*red*), skeleton (*yellow*), and end points (*blue*). Fibril length is quantified as the maximum end-to-end distance of the image skeleton. Scale bars, 5 μm. (*C*) Composite image of a cell on mPADs, used to quantify cell-generated traction forces. (*Red*) Actin; (*white*) mPAD posts; (*green*) FN. Scale bars, 50 μm. (*D*) Comparison of in silico (*red*) and in vitro (*black*) FN fibril length. Standard error bars too small to be visible. (*E*) Comparison of in silico and in vitro normalized force data. In silico and in vitro measurements normalized to a maximum of 155.7 and 6.2 pN, respectively. In (*D*) and (*E*), error bars denote the standard error. To see this figure in color, go online.

element between the cell and the substrate. In this study we develop, to our knowledge, a novel model of cell-matrix-substrate interactions which reproduces the assembly of fibrils of the ECM protein FN. Simulations predict FN fibrils with physiologically accurate architecture and mechanical properties. Our model, which predicts FN fibril assembly starting from a first-principles, molecule-by-molecule approach, is, to our knowledge, the first of its kind and can lead to great insights into how the ECM modulates mechanical signals to cells. Importantly, our model reproduces experimental measurements of key morphometrical FN fibril properties, including length and fourfold extensibility in the presence of actomyosin forces, and the duration of FN fibril assembly.

Previous studies have demonstrated that cell differentiation is a function of both tissue stiffness and soluble ligand presentation (11,51), suggesting that cells are integrating mechanical and soluble signals to determine differentiation fate. However, it is still unclear how these signals are integrated. It is possible that the ECM, assembled by cell-generated forces, acts as a critical point of integration. One could hypothesize that because FN assembly is force-dependent, and forces are larger on stiffer surfaces, that FN assembly is more prevalent on stiffer surfaces; however, neither simulations presented here, nor our previously published work (14) support this hypothesis. In contrast, both simulations and experiments show relatively constant FN fibril assembly across a range of elastic moduli, with a slight peak at intermediate modulus values, highlighting that robust ECM assembly is a critical component of cellular mechanical signaling.

The model does, however, demonstrate an important aspect of cell-ECM mechanotransduction dynamics: assembly of FN fibrils allows cells to modify a stiff surface (which would typically be dominated by a frictional slippage regime in which large forces cannot be generated) to seem more like a soft surface, in which elastic elements allow cells to generate larger forces, by inserting highly elastic fibrils between the cell and substrate. Higher forces have been implicated as a critical component in several pathologies, including differentiation and activation on myofibroblasts in fibrotic disease (52–54) and transformation to a malignant phenotype in cancer (17,24,55). The assembly of FN fibrils may play a key role in facilitating these larger forces, and thus could prove an effective target in blocking increased contractile forces in these disease states.

Assembly of FN fibrils has been studied over the last 40 years. Despite significant work, the fundamental mechanism

underlying FN fibrillogenesis is still not understood. Critically, our model facilitates an investigation of the effects of molecular-level binding events on the macroscopic morphometry of FN fibrils and traction forces. As discussed above, the site(s) of FN-FN interactions have been debated. Several of the Type III domains have been implicated as sites of FN-FN binding (reviewed in Schwarzbauer and DeSimone (30)). However, deletion studies have shown that only domain III-10, which contains the arginine-glycine-asparagine integrin binding sequence, is essential for FN assembly (46), which suggests that there are multiple FN-FN binding sites. Our model readily allows us to simulate competing hypotheses for FN-FN interactions, and future studies will determine whether the location and number of FN-FN binding sites dictates changes in the fibril morphometry.

Another area of active debate in FN biology is the mechanism of FN fibril elasticity. Studies have posited that this could be attributed to the unfolding of individual Type III domains (56) and/or the transition of FN from a compact conformation that is observed in solution (57) to an extended conformation (58). In our model, we only represent individual domain opening and neglect any transition from a compact to extended conformation. However, our model clearly demonstrates a maximal fourfold elasticity of fibrils, which is consistent with experimental observations (34). Previous work by the senior author quantified the force needed to open a single Type III domain and argued that the force needed to stretch each domain fourfold is greater than physiologically relevant forces (59). However, this calculation only examined a single FN molecule and did not consider an entire FN fibril, as our current model does. This work demonstrates that by accounting for appropriate FN fibril geometry, in which actomyosin forces are transmitted via multiple integrin binding sites and distributed over a network of FN molecules, we can predict appropriate FN elasticity at physiologically relevant force magnitudes.

The role of the ECM in mediating contractile force transduction to cell surroundings is not well understood. By constructing a computational model of the interface among substrate, ECM components, and the cell contractile machinery, we gain significant insight into how these mechanical events are coregulated. As such, our model represents a significant step toward integrating molecular-level ECM assembly events and macroscale mechanobiology that will dramatically improve our understanding of mechanical signaling in cells.

SUPPORTING MATERIAL

Supporting Materials and Methods, Supporting Results, two figures, two tables, and one movie are available at http://www.biophysj.org/biophysj/supplemental/S0006-3495(17)30241-2.

AUTHOR CONTRIBUTIONS

S.H.W. and C.A.L. conceptualized the model formulation; S.H.W. implemented the model code; D.B.M. collected and analyzed all experimental data; and C.A.L. oversaw model development and experimental data collection.

ACKNOWLEDGMENTS

The authors acknowledge Harold Erickson and Tomoo Ohashi for their input and thoughts during the development of the model.

Research reported in this publication was supported by the National Institute of General Medical Sciences, National Institutes of Health under award No. R01GM115678 and by the Turing High Performance Computing Cluster at Old Dominion University.

SUPPORTING CITATIONS

References (60–72) appear in the Supporting Material.

REFERENCES

1. Jaalouk, D. E., and J. Lammerding. 2009. Mechanotransduction gone awry. *Nat. Rev. Mol. Cell Biol.* 10:63–73.
2. Chen, C. S. 2008. Mechanotransduction—a field pulling together? *J. Cell Sci.* 121:3285–3292.
3. DuFort, C. C., M. J. Paszek, and V. M. Weaver. 2011. Balancing forces: architectural control of mechanotransduction. *Nat. Rev. Mol. Cell Bio.* 12:308–319.
4. Eyckmans, J., T. Boudou, …, C. S. Chen. 2011. A hitchhiker's guide to mechanobiology. *Dev. Cell.* 21:35–47.
5. van Oers, R. F. F., E. G. Rens, …, R. M. Merks. 2014. Mechanical cell-matrix feedback explains pairwise and collective endothelial cell behavior in vitro. *PLOS Comput. Biol.* 10:e1003774.
6. Saez, A., M. Ghibaudo, …, B. Ladoux. 2007. Rigidity-driven growth and migration of epithelial cells on microstructured anisotropic substrates. *Proc. Natl. Acad. Sci. USA.* 104:8281–8286.
7. Lo, C. M., H. B. Wang, …, Y. L. Wang. 2000. Cell movement is guided by the rigidity of the substrate. *Biophys. J.* 79:144–152.
8. Wang, H. B., M. Dembo, …, Y. Wang. 2001. Focal adhesion kinase is involved in mechanosensing during fibroblast migration. *Proc. Natl. Acad. Sci. USA.* 98:11295–11300.
9. Engler, A. J., S. Sen, …, D. E. Discher. 2006. Matrix elasticity directs stem cell lineage specification. *Cell.* 126:677–689.
10. Lam, W. A., L. Cao, …, S. Kumar. 2010. Extracellular matrix rigidity modulates neuroblastoma cell differentiation and N-myc expression. *Mol. Cancer.* 9:35.
11. Yang, M. T., J. Fu, …, C. S. Chen. 2011. Assaying stem cell mechanobiology on microfabricated elastomeric substrates with geometrically modulated rigidity. *Nat. Protoc.* 6:187–213.
12. Olsen, A. L., S. A. Bloomer, …, R. G. Wells. 2011. Hepatic stellate cells require a stiff environment for myofibroblastic differentiation. *Am. J. Physiol. Gastrointest. Liver Physiol.* 301:G110–G118.
13. You, Y., Q. Zheng, …, Z. Ren. 2016. Matrix stiffness-mediated effects on stemness characteristics occurring in HCC cells. *Oncotarget.* 7:32221–32231.
14. Scott, L. E., D. B. Mair, …, C. A. Lemmon. 2015. Fibronectin fibrillogenesis facilitates mechano-dependent cell spreading, force generation, and nuclear size in human embryonic fibroblasts. *Integr. Biol.* 7:1454–1465.

15. Yeung, T., P. C. Georges, …, P. A. Janmey. 2005. Effects of substrate stiffness on cell morphology, cytoskeletal structure, and adhesion. *Cell Motil. Cytoskeleton.* 60:24–34.

16. Leight, J. L., M. A. Wozniak, …, C. S. Chen. 2012. Matrix rigidity regulates a switch between TGF-β1-induced apoptosis and epithelial-mesenchymal transition. *Mol. Biol. Cell.* 23:781–791.

17. Tilghman, R. W., C. R. Cowan, …, J. T. Parsons. 2010. Matrix rigidity regulates cancer cell growth and cellular phenotype. *PLoS One.* 5:e12905.

18. O'Connor, R. S., X. Hao, …, M. C. Milone. 2012. Substrate rigidity regulates human T cell activation and proliferation. *J. Immunol.* 189:1330–1339.

19. Berg, W. A., E. B. Mendelson, …, C. Cohen-Bacrie. 2015. Quantitative maximum shear-wave stiffness of breast masses as a predictor of histopathologic severity. *AJR Am. J. Roentgenol.* 205:448–455.

20. Hayashi, M., Y. Yamamoto, …, H. Iwase. 2015. Associations between elastography findings and clinicopathological factors in breast cancer. *Medicine (Baltimore).* 94:e2290.

21. Mueller, S., and L. Sandrin. 2010. Liver stiffness: a novel parameter for the diagnosis of liver disease. *Hepat. Med.* 2:49–67.

22. Samir, A. E., A. S. Allegretti, …, H. Y. Lin. 2015. Shear wave elastography in chronic kidney disease: a pilot experience in native kidneys. *BMC Nephrol.* 16:119.

23. Chan, C. E., and D. J. Odde. 2008. Traction dynamics of filopodia on compliant substrates. *Science.* 322:1687–1691.

24. Paszek, M. J., N. Zahir, …, V. M. Weaver. 2005. Tensional homeostasis and the malignant phenotype. *Cancer Cell.* 8:241–254.

25. Fu, J., Y. K. Wang, …, C. S. Chen. 2010. Mechanical regulation of cell function with geometrically modulated elastomeric substrates. *Nat. Methods.* 7:733–736.

26. Han, S. J., K. S. Bielawski, …, N. J. Sniadecki. 2012. Decoupling substrate stiffness, spread area, and micropost density: a close spatial relationship between traction forces and focal adhesions. *Biophys. J.* 103:640–648.

27. Califano, J. P., and C. A. Reinhart-King. 2010. Substrate stiffness and cell area predict cellular traction stresses in single cells and cells in contact. *Cell. Mol. Bioeng.* 3:68–75.

28. Saez, A., A. Buguin, …, B. Ladoux. 2005. Is the mechanical activity of epithelial cells controlled by deformations or forces? *Biophys. J.* 89:L52–L54.

29. Bangasser, B. L., S. S. Rosenfeld, and D. J. Odde. 2013. Determinants of maximal force transmission in a motor-clutch model of cell traction in a compliant microenvironment. *Biophys. J.* 105: 581–592.

30. Schwarzbauer, J. E., and D. W. DeSimone. 2011. Fibronectins, their fibrillogenesis, and in vivo functions. *Cold Spring Harb. Perspect. Biol.* 3:a005041.

31. Mao, Y., and J. E. Schwarzbauer. 2005. Fibronectin fibrillogenesis, a cell-mediated matrix assembly process. *Matrix Biol.* 24:389–399.

32. Zhong, C., M. Chrzanowska-Wodnicka, …, K. Burridge. 1998. Rho-mediated contractility exposes a cryptic site in fibronectin and induces fibronectin matrix assembly. *J. Cell Biol.* 141:539–551.

33. Lemmon, C. A., C. S. Chen, and L. H. Romer. 2009. Cell traction forces direct fibronectin matrix assembly. *Biophys. J.* 96:729–738.

34. Ohashi, T., D. P. Kiehart, and H. P. Erickson. 1999. Dynamics and elasticity of the fibronectin matrix in living cell culture visualized by fibronectin-green fluorescent protein. *Proc. Natl. Acad. Sci. USA.* 96:2153–2158.

35. Skorstengaard, K., M. S. Jensen, …, S. Magnusson. 1986. Complete primary structure of bovine plasma fibronectin. *Eur. J. Biochem.* 161:441–453.

36. Petersen, T. E., H. C. Thøgersen, …, S. Magnusson. 1983. Partial primary structure of bovine plasma fibronectin: three types of internal homology. *Proc. Natl. Acad. Sci. USA.* 80:137–141.

37. Erickson, H. P. 1994. Reversible unfolding of fibronectin Type III and immunoglobulin domains provides the structural basis for stretch and elasticity of titin and fibronectin. *Proc. Natl. Acad. Sci. USA.* 91:10114–10118.

38. Abu-Lail, N. I., T. Ohashi, …, S. Zauscher. 2006. Understanding the elasticity of fibronectin fibrils: unfolding strengths of FN-III and GFP domains measured by single molecule force spectroscopy. *Matrix Biol.* 25:175–184.

39. Oberhauser, A. F., C. Badilla-Fernandez, …, J. M. Fernandez. 2002. The mechanical hierarchies of fibronectin observed with single-molecule AFM. *J. Mol. Biol.* 319:433–447.

40. Pierschbacher, M. D., and E. Ruoslahti. 1984. Cell attachment activity of fibronectin can be duplicated by small synthetic fragments of the molecule. *Nature.* 309:30–33.

41. Bell, G. I. 1978. Models for the specific adhesion of cells to cells. *Science.* 200:618–627.

42. Hu, K., L. Ji, …, C. M. Waterman-Storer. 2007. Differential transmission of actin motion within focal adhesions. *Science.* 315:111–115.

43. Jurado, C., J. R. Haserick, and J. Lee. 2005. Slipping or gripping? Fluorescent speckle microscopy in fish keratocytes reveals two different mechanisms for generating a retrograde flow of actin. *Mol. Biol. Cell.* 16:507–518.

44. Ferreira, A. J. M. 2008. MATLAB Codes for Finite Element Analysis. *In* Solids and Structures, *Vol. 157*. Springer Science & Business Media, Dordrecht, The Netherlands.

45. Gao, M., D. Craig, …, K. Schulten. 2003. Structure and functional significance of mechanically unfolded fibronectin Type III1 intermediates. *Proc. Natl. Acad. Sci. USA.* 100:14784–14789.

46. Schwarzbauer, J. E. 1991. Identification of the fibronectin sequences required for assembly of a fibrillar matrix. *J. Cell Biol.* 113:1463–1473.

47. Gao, M., D. Craig, …, K. Schulten. 2002. Identifying unfolding intermediates of FN-III(10) by steered molecular dynamics. *J. Mol. Biol.* 323:939–950.

48. Bustamante, C., J. F. Marko, …, S. Smith. 1994. Entropic elasticity of λ-phage DNA. *Science.* 265:1599–1600.

49. Marko, J. F., and E. D. Siggia. 1995. Stretching DNA. *Macromolecules.* 28:8759–8770.

50. Singer, I. I., D. W. Kawka, …, R. A. Clark. 1984. In vivo co-distribution of fibronectin and actin fibers in granulation tissue: immunofluorescence and electron microscope studies of the fibronexus at the myofibroblast surface. *J. Cell Biol.* 98:2091–2106.

51. Buxboim, A., and D. E. Discher. 2010. Stem cells feel the difference. *Nat. Methods.* 7:695–697.

52. Hinz, B., and G. Gabbiani. 2003. Mechanisms of force generation and transmission by myofibroblasts. *Curr. Opin. Biotechnol.* 14:538–546.

53. Hinz, B., and G. Gabbiani. 2003. Cell-matrix and cell-cell contacts of myofibroblasts: role in connective tissue remodeling. *Thromb. Haemost.* 90:993–1002.

54. Hinz, B., S. H. Phan, …, G. Gabbiani. 2007. The myofibroblast: one function, multiple origins. *Am. J. Pathol.* 170:1807–1816.

55. Kraning-Rush, C. M., J. P. Califano, and C. A. Reinhart-King. 2012. Cellular traction stresses increase with increasing metastatic potential. *PLoS ONE.* 7:e32572.

56. Smith, M. L., D. Gourdon, …, V. Vogel. 2007. Force-induced unfolding of fibronectin in the extracellular matrix of living cells. *PLoS Biol.* 5:e268.

57. Johnson, K. J., H. Sage, …, H. P. Erickson. 1999. The compact conformation of fibronectin is determined by intramolecular ionic interactions. *J. Biol. Chem.* 274:15473–15479.

58. Erickson, H. P. 2002. Stretching fibronectin. *J. Muscle Res. Cell Motil.* 23:575–580.

59. Lemmon, C. A., T. Ohashi, and H. P. Erickson. 2011. Probing the folded state of fibronectin Type III domains in stretched fibrils by measuring buried cysteine accessibility. *J. Biol. Chem.* 286:26375–26382.

60. Gillespie, D. T. 1977. Exact stochastic simulation of coupled chemical reactions. *J. Phys. Chem.* 81:2340–2361.

61. Alfonsi, A., E. Cancès, …, W. Huisinga. 2005. Adaptive simulation of hybrid stochastic and deterministic models for biochemical systems. *ESAIM.* 14:1–13.

62. Nivala, M., E. de Lange, …, Z. Qu. 2012. Computational modeling and numerical methods for spatiotemporal calcium cycling in ventricular myocytes. *Front. Physiol.* 3:114.

63. Lele, T. P., C. K. Thodeti, …, D. E. Ingber. 2008. Investigating complexity of protein-protein interactions in focal adhesions. *Biochem. Biophys. Res. Commun.* 369:929–934.

64. Fisher, T. E., A. F. Oberhauser, …, J. M. Fernandez. 1999. The study of protein mechanics with the atomic force microscope. *Trends Biochem. Sci.* 24:379–384.

65. Jiang, G., G. Giannone, …, M. P. Sheetz. 2003. Two-piconewton slip bond between fibronectin and the cytoskeleton depends on talin. *Nature.* 424:334–337.

66. Umemoto, S., A. R. Bengur, and J. R. Sellers. 1989. Effect of multiple phosphorylations of smooth muscle and cytoplasmic myosins on movement in an in vitro motility assay. *J. Biol. Chem.* 264:1431–1436.

67. Cuda, G., E. Pate, …, J. R. Sellers. 1997. In vitro actin filament sliding velocities produced by mixtures of different types of myosin. *Biophys. J.* 72:1767–1779.

68. Molloy, J. E., J. E. Burns, …, D. C. White. 1995. Movement and force produced by a single myosin head. *Nature.* 378:209–212.

69. McDonough, J. 1985. Plasma Fibronectin. Structure and Functions. CRC Press, Boca Raton, FL.

70. Berg, J. M., J. L. Tymoczko, and L. Stryer. 2002. Biochemistry. W. H. Freeman, New York.

71. Leahy, D. J., I. Aukhil, and H. P. Erickson. 1996. 2.0 Å crystal structure of a four-domain segment of human fibronectin encompassing the RGD loop and synergy region. *Cell.* 84:155–164.

72. Ylätupa, S., C. Haglund, …, P. Partanen. 1995. Cellular fibronectin in serum and plasma: a potential new tumour marker? *Br. J. Cancer.* 71:578–582.

Biophysical Journal, Volume *112*

Supplemental Information

Mechanotransduction Dynamics at the Cell-Matrix Interface

Seth H. Weinberg, Devin B. Mair, and Christopher A. Lemmon

Supporting Material for "Mechanotransduction Dynamics at the Cell-Matrix Interface"

S. H. Weinberg, D. B. Mair, C. A. Lemmon

SUPPORTING METHODS

Description of the elastic-stochastic model of FN fibril assembly

In this study, we develop a computational model of fibronectin (FN) fibril assembly and cell-FN fibril-substrate interactions. Our model expands on a prior elastic-stochastic model developed by Chan and Odde (1). In brief, the Chan-Odde model represents a stochastic motor-clutch system, in which traction forces are generated by molecular clutch "engagement" via integrin binding, linking actomyosin forces to the extracellular substrate. Molecular clutches and the substrate are represented by Hookean springs. Most critically distinct from our model described below, in the Chan-Odde model, actomyosin force transmission through engaged elastic molecular clutches occurs directly to the substrate, and the Chan-Odde model does not specifically account for elasticity of and force transmission via ECM proteins at the cell-matrix-substrate interface.

In our model, each FNIII domain is represented by a time-varying Hookean spring (Figure 1A), with spring constant $k_i^j(t)$, where $i \in \{1, \cdots, 30\}$, $j \in \{1, \cdots, N_{FN}(t)\}$ are Type III domain and FN molecule indices, respectively and $N_{FN}(t)$ is the total number of FN molecules in the growing FN fibril and is a function of time t. The FN dimer is comprised of 30 FNIII domains, such that each FN molecule is represented by 30 springs in series. FNI and FNII domains are assumed to be inelastic and non-stretchable. As FN-FN binding occurs during assembly as described below, FN-FN connections are formed between one of the 30 FNIII domains and the N-terminus of a new FN molecule. Thus, the growing fibril is represented by a Hookean spring network with complex architecture defined by the specific FN-FN connections.

Actomyosin forces are transmitted to the assembling FN fibril via integrin connections between the cell surface and the fibril. FNIII-10 bind the $\alpha_5\beta_1$ integrin, which links the FN molecule to a focal adhesion complex (FAC) and transmits actin-dependent force. Extracellular and intracellular signaling within the integrin-FAC-actin system is complex and representing these signaling interactions is beyond the scope of our present model. Following the approach by Chan and Odde (1), we represent the FNIII-10-integrin-FAC-actin connection by a single Hookean spring with spring constant k_c and refer to this connection as a "molecular clutch" (Figure 1A, green springs). Clutch "engagement"/"disengagement" is stochastic and force-dependent. Actomyosin forces, transmitted via engaged clutches, stretch individual FNIII domains (Figure 1B), facilitating the binding of new FN molecules (Figure 1C, red lines). The proba-

bility of FN molecule addition increases with FNIII domain stretch and is also a function of soluble FN concentration. Subsequent integrin binding occurs at the new FN molecule, and the process of FN molecule addition continues until an insoluble, elastic FN fibril is formed (Figure 1D).

Thus, each FN molecule consists of a spring network of 32 springs (30 FNIII domains and 2 clutches). The total number of springs in the FN fibril network at time t is $N^T_{spring}(t) = 32N_{FN}(t) + 1$, where the additional spring represents the substrate (with spring constant k_{sub}), and finally the total number of nodes in the spring network is $N^T_{node}(t) = N^T_{spring}(t) + 1$.

FNIII domain and molecular clutch forces

We define u^j_i as the displacement of the (i,j)-th domain node from its equilibrium position along the z-axis, i.e. displacement in the absence of force. The domain spring constant $k^j_i(t)$ and force $f^j_i(t)$ in the (i,j)-th domain are related to the domain node displacements $u^j_i(t)$ and $u^j_{i+1}(t)$ by Hooke's law,

$$f^j_i = k^j_i(u^j_{i+1} - u^j_i) = k^j_i \epsilon^j_i, \tag{S1}$$

where $\epsilon^j_i = u^j_{i+1} - u^j_i$ is the elongation or stretch of the (i,j)-th FNIII domain. Similarly, the clutch spring constant k_c and force $f^j_{c,m}(t)$ in the (m,j)-th clutch are related by

$$f^j_{c,m} = k_c(u^j_{c,m} - u^j_{10m+1}), \tag{S2}$$

where $m \in \{1,2\}$ is the index of the clutch and $u^j_{c,m}(t)$ is the displacement of the (m,j)-th clutch node from its equilibrium position. The displacement $u^j_{10m+1}(t)$ represents the displacement of the two FNIII-10 domains in the j-th FN dimer, with indices 11 and 21, respectively. The displacement of the substrate spring nodes are given by $u_{sub,0}$ and $u_{sub,1}$, where one end of the spring is "fixed," i.e., $u_{sub,0} = 0$ is an imposed relationship, or boundary condition, and the other substrate spring node is attached to FNIII-1 of the first FN dimer, i.e., $u_{sub,1} = u^1_1$. Thus, the elongation or stretch of the substrate $\epsilon_{sub} = u_{sub,1} - u_{sub,0} = u_{sub,1} = u^1_1$. For ease of notation later, we define $u^1_0 = u_{sub,0} = 0$.

Integrin binding

Integrin binding, i.e., molecular clutch engagement/disengagement, reactions for the (m,j)-th clutch are represented by a first-order reversible reaction,

$$\text{(disengaged) } \mathcal{D} \underset{\bar{\nu}^j_{m,off}}{\overset{\nu_{on}}{\rightleftharpoons}} \mathcal{E} \text{ (engaged)}, \tag{S3}$$

where ν_{on} and $\bar{\nu}^j_{m,off}$ are rates with units of inverse time. Engaged clutches build tension, as the connection via the clutch spring is stretched by actin motion. The

tension in engaged clutches increases the off-rate $\bar{\nu}^j_{m,off}$ exponentially, following a Bell model (2),

$$\bar{\nu}^j_{m,off} = \nu_{off} \exp(f^j_{c,m}/f_b), \tag{S4}$$

where ν_{off} is the disengagement rate in the absence of clutch displacement and f_b is a break force. Thus as $f^j_{c,m}$ increases (Eq. S2), the disengagement rate increases, and the clutch bond becomes more likely to break.

Actomyosin-dependent FN fibril stretch

We assume that actomyosin forces will slow when acting against an elastically loaded substrate according to a linear force-velocity relationship (1),

$$v_{act} = v_u \left(1 - \frac{k_{sub}\epsilon_{sub}}{f_{stall}}\right), \tag{S5}$$

where v_{act} is the actin velocity, v_u is the unloaded actin velocity, ϵ_{sub} is the displacement of the substrate, and $f_{stall} = N_{myo}f_{myo}$ is a stall force that is given by the number of myosin motors N_{myo} and unitary myosin motor force f_{myo}. When substrate force $f_{sub} = k_{sub}\epsilon_{sub}$ is equal to the stall force f_{stall}, the actin filament "stalls," terminating FN assembly.

If we define $\sigma^j_{c,m} \in \{0, 1\}$ as the state of the (m, j)-th molecular clutch, such that $\sigma^j_{c,m} = 0$ or 1 when the clutch is disengaged or engaged, respectively, then the time-dependent dynamics of the clutch displacement $u^j_{c,m}$ is given by

$$\frac{du^j_{c,m}}{dt} = \sigma^j_{c,m} v_{act}. \tag{S6}$$

FNIII domain and molecular clutch node displacement

The temporal dynamics of the displacement of engaged clutches are given by Eq. S6, which in turn transmits actomyosin forces that alter the position of all nodes in the spring network. We assume that FNIII domain node positions are in a rapid equilibrium, such that node positions can be solved by the direct stiffness method, a standard finite element method approach (3). Formally, we solve the linear system given by

$$\mathbf{K}\boldsymbol{u} = \boldsymbol{f}, \tag{S7}$$

where $\mathbf{K}(t)$ is the $N^T_{node} \times N^T_{node}$ global stiffness matrix assembled from the time-dependent spring constants $k^j_i(t)$, $\boldsymbol{u}(t)$ is the $N^T_{node} \times 1$ column vector of displacements

$$\boldsymbol{u} = (u^1_0, u^1_1, \cdots, u^1_{30}, u^1_{c,1}, u^1_{c,2}, u^2_1, \cdots, u^{N_{FN}}_{30}, u^{N_{FN}}_{c,1}, u^{N_{FN}}_{c,2})^T,$$

and $\boldsymbol{f}$ is a $N^T_{node} \times 1$ column vector of external forces.

The engaged clutch displacement(s) and fixed substrate position are imposed as boundary conditions on Eq. S7, which introduces non-zero elements in $\boldsymbol{f}_{red}$, resulting in the reduced linear system,

$$\mathbf{K}_{red}\boldsymbol{u}_{red} = \boldsymbol{f}_{red}. \tag{S8}$$

and the position of the nodes are given by $\boldsymbol{u}_{red} = \mathbf{K}_{red}^{-1}\boldsymbol{f}_{red}$.

Time-varying FNIII domain spring constants

Each FNIII domain is represented by a time-varying Hookean spring. In the absence of actomyosin forces, each FNIII domain spring constant k_i^j is equal to a unique spring constant $k_{i,0}$ (see Table S2), representing the unique mechanical properties of each FNIII domain, while in the presence of large actomyosin forces, domain stiffness values are governed by a worm-like chain (WLC) model, which accounts for the highly nonlinear increase in domain stiffness k_i^j as domain elongation ϵ_i^j increases (4, 5). Recent studies have demonstrated that the WLC model yields similar predictions to molecular dynamics simulations of protein unfolding under high force (6).

The WLC model relates the molecular force F_ω and stretch or elongation ϵ by the following equation:

$$F_\omega(\epsilon) = \left(\frac{k_B T}{\chi_p}\right)\left[\frac{1}{4(1-\epsilon/\chi_d)^2} - \frac{1}{4} + \frac{\epsilon}{\chi_d}\right], \tag{S9}$$

where k_B is Boltmann's constant, T is the absolute temperature, χ_p is the domain persistant length, and χ_d is the domain contour length. To relate this WLC model to the spring network that is the basis of our model, we define the spring constant k_ω relating the force F and displacement ϵ of spring from rest as the derivative of F_ω in Eq. S9, with respective to ϵ,

$$k_\omega(\epsilon) = \frac{dF_\omega}{d\epsilon} = \left(\frac{k_B T}{\chi_d \chi_p}\right)\left[\frac{1}{2(1-\epsilon/\chi_d)^3} + 1\right]. \tag{S10}$$

We model the time-varying domain stiffness $k_i^j(t)$ as a first-order isomerization reaction, such that $k_i^j(t)$ exponentially relax to a domain stretch-dependence steady-state domain stiffness $k_i^\infty(\epsilon_i^j)$, with time constant τ_ω,

$$\frac{dk_i^j}{dt} = \frac{k_i^\infty(\epsilon_i^j) - k_i^j}{\tau_\omega}. \tag{S11}$$

The steady-state domain stiffness k_i^∞ transitions between the ϵ_i^j-dependent regimes for unique stiffnesses and the (identical) WLC-governed stiffnesses, i.e., $k_i^\infty(0) = k_{i,0}$, and for large ϵ_i^j, $k_i^\infty(\epsilon_i^j)$ approaches $k_\omega(\epsilon_i^j)$ (see Figure 3),

$$\hat{k}_i^\infty(\epsilon_i^j) = k_\omega(\epsilon_i^j) + [k_{i,0} - k_\omega(0)]\exp(-\epsilon_i^j/\lambda_\omega), \tag{S12}$$

where λ_ω is a space constant that defines the regime transition. Finally, since $k_\omega(\epsilon) \to \infty$ as $\epsilon \to \chi_d$, for numerical stability, we define a maximum domain stiffness k_{max} and define k_i^∞ as the minimum value of k_{max} and $\hat{k}_i^\infty(\epsilon_i^j)$.

Soluble FN binding and fibril assembly

In our model, FN binding is treated as a two-step process: binding sites are exposed via a stretch-dependent mechanism and soluble FN binds to an exposed binding site. We assume that for the (i,j)-th domain, the probability of FN binding site exposure π_i^j is a function of domain stretch ϵ_i^j and given by a Hill-type equation,

$$\pi_i^j = \frac{(\epsilon_i^j)^\eta}{(\epsilon_i^j)^\eta + \epsilon_t^\eta}, \tag{S13}$$

where ϵ_t is the stretch-dependent threshold, in units of length, and η is a scaling factor that determines the threshold steepness.

Following binding site exposure, an irreversible reaction between soluble FN, $\mathcal{S}$, and the exposed binding site, Δ_i^j, resulting in FN-FN binding, $\mathcal{B}_i^j$, at the (i,j)-th domain:

$$\mathcal{S} + \Delta_i^j \xrightarrow{\nu_{FN}} \mathcal{B}_i^j, \tag{S14}$$

a reaction that occurs with a rate of $\nu_{FN}[\mathcal{S}]$, where $[\mathcal{S}]$ is the concentration of soluble FN in the extracellular space.

FN fibril geometry

The Hookean spring network is 1-dimensional, with actomyosin forces and FNIII domain and clutch displacements occurring along with the z-axis. However, we account for the location of each FN molecule in the (x,y)-plane, assuming that the FN fibril assembles via hexagonal packing with spacing $2r$, where r is the radius of each FN molecule, modeled as a 3-dimensional cylinder. Thus, each FN molecule has a maximum of 6 "neighbors" in the (x,y)-plane. Once the j-th FN molecule has 6 neighbors, either via its own connections or connections of its neighbors, the FN molecule is consider an "interior" FN molecule and can no longer make additional FN-FN connections. Further, we assume that FN-FN bonds do not break once formed.

Importantly, the FNIII-10 integrin binding sites of interior FN molecule are no longer exposed to the cell surface. To account for the inaccessibility of these molecular clutches, we set the clutch engagement rate $\nu_{m,on}^j = 0$ for these FN molecules.

Simulations and analysis

Numerical simulations are performed for 30 hours or until assembly is terminated by "stalled" actomyosin forces (see Eq. S5). For each simulation, we measure the size of the terminal FN fibril (stretched/relaxed length, thickness, number of FN molecules), as well as traction forces and clutch engagement. For the baseline parameter set ($k_{sub} = 1000$ pN/nm), we run 500 simulations, and for all other k_{sub} values, we run 100 simulations.

Numerical simulation implementation

Overview of the hybrid deterministic-stochastic simulation algorithm

Simulation of FN fibril assembly involves time scales ranging over several orders of magnitude: Molecular clutch engagement/disengagement are stochastic events occurring on the order of milliseconds, while FN fibril assembly occurs on the order of hours to days. In order to simulate fibril assembly, we utilize a multiscale hybrid stochastic-deterministic integration scheme that enables the use of a relatively large numerical integration time step, while still appropriately accounting for clutch engagement/disengagement stochastic events.

In general, in order to simulation the stochastic chemical interactions of a system of chemical species interacting via elementary processes (i.e., biochemical reactions), we compute the *propensity function* for each reaction $a_q(\boldsymbol{X}(t))$, which has the property that, to first-order, the probability $p_q(t)$ of the *q-th* reaction taking place in the infinitesimal time interval $[t, t + dt)$ is given by $p_q(t) = a_q(\boldsymbol{X}(t))dt$, where vector $\boldsymbol{X}(t)$ collects the state of all chemical species. For a stochastic simulation with fixed time step to be meaningful, $p_q(t)$ must be less than 1, and further $p_q(t)$ must be small, typically 0.01-0.05, such that the system dynamics do not change significantly within a single time step. This requirement places an strict limitation on the time step dt chosen. For the clutch engagement/disengagement reversible reaction for the (m, j)-*th* clutch (Eq. S3), the individual elementary processes, $\mathcal{D} \rightarrow \mathcal{E}$ and $\mathcal{E} \rightarrow \mathcal{D}$, have propensity functions given by $a_1 = \nu^j_{m,on}(1 - \sigma^j_{c,m})$ and $a_2 = \bar{\nu}^j_{m,off}\sigma^j_{c,m}$, respectively. In order to avoid using a prohibitively small time step, we use the stochastic simulation algorithm, also known as Gillespie's method, which is an exact algorithm without an inherent time step (7).

In brief, Gillespie's method is an iterative stochastic algorithm in which random numbers are drawn in order to determine the time until the next reaction occurs and which reaction occurs at that time. If $a_{sum}(\boldsymbol{X}(t)) = \sum_q a_q(\boldsymbol{X}(t))$, then the time until the next reaction occurring τ is given by

$$a_{sum}(\boldsymbol{X}(t))\tau = \xi, \tag{S15}$$

where ξ is an exponentially distributed random variable (r.v.), which in practice can be determined by drawing an uniformly distributed r.v. U_1 and defining $\xi = -\ln U_1$. If there multiple possible reactions, then the reaction that occurs after time τ, reaction n, is given by the smallest integer n that satisfies

$$\frac{\sum_q^n a_q(\boldsymbol{X}(t))}{a_{sum}(\boldsymbol{X}(t))} < U_2, \tag{S16}$$

where U_2 is a different uniformly distributed r.v.

This method is strictly valid with the constraint that the propensity functions remain constant over the time interval $[t, t + \tau)$. However, from Eqs. S2

and S4, it is clear that $\bar{\nu}^j_{m,off}$ is function of the clutch and domain node displacements and therefore a function of time. In this case, Eq. S15 should be replaced with

$$\int_t^{t+\tau} a_{sum}(\boldsymbol{X}(t'))dt' = \xi, \tag{S17}$$

where τ is time until the next reaction (8). In practice, we utilize a hybrid scheme (9), in which we define a global time step Δt (such that number of total global time steps $N_{global} = T_{total}/\Delta t$ and T_{total} is the total simulation time). During each time step, we treat node displacement values as constant, which simplifies the use of Eq. S17 to determine clutch engagement/disengagement events. At the end of each global time step, we update node displacements using Eqs. S6 and S8, as described below.

Simulations are performed with a global time step $\Delta t = 5$ ms, for a duration of 30 hours ($N_{global} = 2.16 \cdot 10^7$ steps) or until actomyosin forces stall (described below). In the following subsections, we describe the initialization, iteration, and termination of the stochastic simulation of FN assembly.

Initialization

At the initial time point, we assume that one FN molecule is connected to the substrate, and both molecules clutches are disengaged. The initial conditions for the simulation are given as follows:

- Initial domain displacements: $u_{sub} = u^1_1 = u^1_2 = \cdots = u^1_{30} = 0$,
- Initial clutch displacements: $u^1_{c,1} = u^1_{c,2} = 0$,
- Initial clutch state: $\sigma^1_{c,1} = \sigma^1_{c,2} = 0$,
- Initial stiffness vector: $\boldsymbol{k} = (k_{sub}, k^1_1, k^1_2, \cdots, k^1_{30}, k_c, k_c)^T \equiv \boldsymbol{k}_0$,
- Initial total number of FN molecules: $N_{FN} = 1$,
- Initial exponential r.v. and previous value P: $\xi = -\ln(U)$, $P = 0$ (see below), where U is a uniform r.v.
- Initial global time: $t_{global} = 0$,
- Initial set of network connection defining architecture: $S_{\mathcal{A}} = \{\emptyset\}$
- A connection matrix A_{conn}, of size $N^T_{spring} \times 2$, is initialized that defines the spring network architecture. Each row corresponds to one spring in the network and columns indicate the (i, j)-th node indices of the spring

endpoints. Thus, the initial value for A_{conn} is given by

$$A_{conn} = \begin{pmatrix} (0,1) & (1,1) \\ (1,1) & (2,1) \\ \vdots & \vdots \\ (30,1) & (31,1) \\ (10,1) & (c1,1) \\ (20,1) & (c2,1) \end{pmatrix},$$

where $c1$ and $c2$ are the indices of the two molecular clutches. The global stiffness matrix $\mathbf{K}$ is initialized using $\boldsymbol{k}$ and A_{conn}.

Note that we define $S_{\mathcal{A}}(t)$ as the ordered sequence or list of FN-FN connections, where by construction the $q\text{-}th$ element of $S_{\mathcal{A}}$ is the index (i,j) of the FN binding site for FN molecule q, at time t. For example, if at some time point t,

$$S_{\mathcal{A}}(t) = \langle \emptyset, (2,1), (4,1), (1,2) \rangle,$$

then, the second FN molecule (in order of assembly), is bound to FNIII-2 (domain 2) of the first FN molecule, which is bound to the substrate. The third FN molecule is connected to FNIII-4 of the first FN molecule, and the fourth FN molecule is connected to FNIII-1 of the second FN molecule. The first FN molecule does not have a FN-FN connection (being connected to the substrate), and by convention we define this connection as the empty set $\emptyset$. Thus, $S_{\mathcal{A}}(t)$ fully defines the architecture of the spring network. Note that the total number of FN molecule in the FN fibril at time t, $N_{FN}(t) = n(S_{\mathcal{A}}(t))$, the number of elements in $S_{\mathcal{A}}(t)$.

Iteration

The following calculations are performed for N_{global} steps and simulation state variables are output at the desired time points:

1. FNIII domain node displacement: After applying the appropriate boundary conditions, the reduced linear system vectors ($\mathbf{K}_{red}$ and $\boldsymbol{f}_{red}$) are determined from the full system ($\mathbf{K}$ and $\boldsymbol{f}$), and the reduced system is solved numerically (Eq. S8):

$$\boldsymbol{u}_{red} = \mathbf{K}_{red}^{-1} \boldsymbol{f}_{red}. \tag{S18}$$

   Domain node displacements u_i^j are updated accordingly from the values in $\boldsymbol{u}_{red}$.

2. Molecular clutch engagement/disengagement: Clutch engagement/disengagement is represented by a reversible first-order reaction (Eq. S3). Each FN molecule has two possible clutch binding sites, at domains 11 and 21, and therefore, there are $2N_{FN}$ clutches in the growing fibril. As discussed

above, we use a modified version of Gillespie's method to simulation clutch engagement/disengagement events:

At the beginning of each global time step, we define a local time $t_{local} = 0$ and perform the following:

- Define the propensity functions for all (m, j)-th clutch (dis)engagement events, for $m \in \{1, 2\}$ and $j \in \{1, 2, \cdots, N_{FN}\}$:
  - For engagement events $\mathcal{D} \to \mathcal{E}$: $a_q = \nu^j_{m,on}(1 - \sigma^j_{c,m})$, for $q = 2(j-1) + m$.
  - For disengagement events $\mathcal{E} \to \mathcal{D}$: $a_q = \bar{\nu}^j_{m,off}\sigma^j_{c,m}$, for $q = 2(j-1) + m + 2N_{FN}$, where $\bar{\nu}^j_{m,off}$ is given by Eq. S4.
- Define $a_{sum} = \sum_q a_q$.
  While $t_{local} < \Delta t$
  - *If* $(\xi - P) \leq a_{sum}\Delta t$ (reaction occurs within global time step)
    - The time to next reaction $\tau \leftarrow \xi / a_{sum}$ (Eq. S15).
    - Previous value reset to zero: $P \leftarrow 0$.
    - The index of reaction n that occurs is given by the smallest integer n that satisfies $\sum_q^n a_q < U \cdot a_{sum}$ (Eq. S16), where U is a uniformly distributed r.v.
      - *If* $n \leq 2N_{FN}$ (engagement event occurs): $\sigma^j_{c,m} \leftarrow 1$, where $j = \lceil n/2 \rceil$ and $m = n - 2(j-1)$.
      - *Else if* $n > 2N_{FN}$ (disengagement event occurs): $\sigma^j_{c,m} \leftarrow 0$, where $j = \lceil (n - 2N_{FN})/2 \rceil$ and $m = n - 2(j-1) - 2N_{FN}$.
    - *If* $t_{local} + \tau \leq \Delta t$ (local time remains within the global time step)
      - Draw new exponential r.v.: $\xi \leftarrow -\ln(U)$
      - Update local time: $t_{local} \leftarrow t_{local} + \tau$
    - *Else if* $t_{local} + \tau > \Delta t$ (local time exceeds global time step)
      - Draw new exponential r.v.: $\xi \leftarrow -\ln(U) - a_{sum}(\Delta t - t_{local})$
      - Update local time to break loop: $t_{local} \leftarrow \Delta t$
  - *Else if* $(\xi - P) > a_{sum}\Delta t$ (no reaction occurs in global time step)
    - Update previous value: $P \leftarrow P + a_{sum}\Delta t$
    - Update local time to exit *while* loop: $t_{local} \leftarrow \Delta t$

3. Clutch node displacement: Engaged clutch node displacements are updated by numerical integration of Eq. S6 using the forward Euler method:

$$u^j_{c,m} \leftarrow u^j_{c,m} + v_{act}\Delta t, \text{ for all } (m, j) \in S_{\mathcal{E}}, \tag{S19}$$

where actin velocity v_{act} is given by Eq. S5, and $S_{\mathcal{E}}$ is the set of the indices of the engaged clutches, $S_{\mathcal{E}} = \{(m, j) \mid \sigma^j_{c,m} = 1\}$. Note that the

first-order Euler integration method is exact, since v_{act} is constant over each global time step.

By definition, the force in a disengaged clutch $f_{c,m}^j$ is equal to zero. Therefore, the displacement of the disengaged clutch node is given by (Eq. S2)

$$u_{c,m}^j \leftarrow u_{10m+1}^j, \text{ for all } (m,j) \in S \backslash S_{\mathcal{E}}, \tag{S20}$$

where S is the set of all appropriate values of (m,j) and $S \backslash S_{\mathcal{E}} = \{(m,j) \mid \sigma_{c,m}^j = 0\}$ is the set of all disengaged clutches.

4. Time-varying domain stiffnesses: Domain stiffnesses k_i^j are updated by numerical integration of Eq. S11 using the fourth-order Runge Kutta method (RK4):

$$k_i^j \leftarrow k_i^j + \frac{\Delta t}{6}\left(\theta_1 + 2\theta_2 + 2\theta_3 + \theta_4\right), \tag{S21}$$

where $\theta_1 = \mathcal{F}_\Omega(k_i^j, \epsilon_i^j)$, $\theta_2 = \mathcal{F}_\Omega(k_i^j + \frac{1}{2}\theta_1, \epsilon_i^j)$, $\theta_3 = \mathcal{F}_\Omega(k_i^j + \frac{1}{2}\theta_2, \epsilon_i^j)$, $\theta_4 = \mathcal{F}_\Omega(k_i^j + \theta_3, \epsilon_i^j)$, and $\mathcal{F}_\Omega(k_i^j, \epsilon_i^j) = (k_i^\infty(\epsilon_i^j) - k_i^j)/\tau_\omega$. The appropriate values in stiffness vector $\boldsymbol{k}$ are updated.

5. FN-FN binding: We define $\phi_i^j \in \{0,1\}$ as the state of (i,j)-th domain, such that $\phi_i^j = 0$ (1) when the domain is not bound (is bound) to a FN molecule. We further define the "neighbor" function $\mathcal{F}_n(j) : j \to \mathcal{N}$, where $\mathcal{N} \in \{1, 2, \cdots, 6\}$ is the number of neighbors for the j-th FN molecule.

   - For every FNIII domain, a uniformly distributed r.v. U_i^j is drawn.

   - *If* $\phi_i^j = 0$ (domain is unbound) AND $U_i^j < \pi_i^j$ (binding site is exposed, Eq. S13) AND $\mathcal{F}_n(j) < 6$ (a new FN molecule can bind)
     - Draw a new uniformly distributed r.v. U
     - *If* $U < \nu_{FN}[\mathcal{S}]\Delta t$ (Eq. S14, new FN-FN connection is formed): A connection between the (i,j)-th domain and a new FN molecule is added to the growing fibril. Initialize and update the following:
       * Domain state is occupied: $\phi_i^j = 1$,
       * Increase total number of FN molecules: $N_{FN} \leftarrow N_{FN} + 1$,
       * Initialize clutch states: $\sigma_{c,1}^{N_{FN}} = \sigma_{c,2}^{N_{FN}} = 0$,
       * Update stiffness vector: $\boldsymbol{k} \leftarrow (\boldsymbol{k}^T, \boldsymbol{k}_0)^T$
       * Update architecture ordered set: $S_{\mathcal{A}} \leftarrow \langle S_{\mathcal{A}}, (i,j) \rangle$

* Update connection matrix: $A_{conn} \leftarrow \begin{pmatrix} A_{conn} & \\ (1, N_{FN}) & (2, N_{FN}) \\ \vdots & \vdots \\ (30, N_{FN}) & (31, N_{FN}) \\ (10, N_{FN}) & (c1, N_{FN}) \\ (20, N_{FN}) & (c2, N_{FN}) \end{pmatrix}$
  By construction, the index of the first domain of the new FN dimer $(1, N_{FN})$ is equal to the index of the FN-FN connection (i, j).
* *If* FN dimer j has become an interior dimer as discussed above, i.e., $\mathcal{F}_n(j) = 6$: set clutch engagement rates to zero as described above.
* Global stiffness matrix: The global stiffness matrix $\mathbf{K}$ is updated using current values of $\boldsymbol{k}$ and A_{conn}.

6. Global time: The global time step is updated:

$$t_{global} \leftarrow t_{global} + \Delta t. \tag{S22}$$

Termination

- End simulation *if* $t_{global} = T_{total}$ *OR* $v_{act} < 0.005 v_u$ (Actomyosin forces "stall").

Model parameters

Values and the sources for the model parameters are given in the following two tables. Molecular clutch, substrate, and actin parameters are given in Table S1. Most model parameters were based on values given in Chan and Odde (1).

In Table S2, parameter values for the FN Type III domain stiffness values and other FN fibril parameters are given. Several parameters were estimated based on reasonable approximations and estimations from the literature: In order to estimate the resting stiffness values of the FN Type III domains, we first assumed that the resting stiffness values for all FNIII domains were less than the molecular clutch stiffness k_c of 5 pN/nm (from Chan and Odde (1)), such that FN binding events could occur before clutch disengagement events became highly probable. We then estimated the relative mechanical stiffness from recent atomic force microscopy (10), buried cysteine assays (11), and protein denaturation assays (personal communication with Tomoo Ohashi and Harold Erickson).

The domain stiffness relaxation time constant τ_ω was estimated to approximately match the relaxation of the length measurement to its steady-state value and to match the approximate duration for fibril assembly. The domain stiffness space constant λ_ω was estimated such that the elongation-dependent stiffness values were distinct at the domain binding site exposure threshold ϵ_t and comparable for elongations approximately twice ϵ_t (see Figure 3).

To estimate the soluble FN binding rate, ν_{FN}, we assumed that soluble FN binding to an exposed FN binding site is diffusion-limited (i.e., the elementary binding reaction is rapid), then $\nu_{FN} \approx 4\pi r_{FN} D_{FN} N_A$, where $r_{FN} = 9$ nm is the soluble FN fibril radius (12), D_{FN} is the FN diffusion coefficient, and N_A is Avogadro's constant. Based on diffusion rates for plasma FN ($D_{FN} = 2.5 \cdot 10^{-7}$ cm^2 s^{-1}, (12)) and membrane-bound FN ($D_{FN} = 0.7 \cdot 10^{-12}$ cm^2 s^{-1}, (13)) as upper and lower limits, respectively, such that ν_{FN} may range over $4.7 \cdot 10^{-6} - 1.7$ nM^{-1} s^{-1}, we choose an intermediate value of 0.001, assuming that soluble FN diffusion is partially restricted due to the close proximity of the assembling fibril. The domain binding site exposure scaling factor η was chosen to be 6, based on the Hill coefficient for cooperative binding assuming 6 possible binding sites for a hexagonal packing structure for the assembling fibril.

SUPPORTING RESULTS

Number of fibronectin molecules predicts fibril morphometrical and mechanical properties in a substrate-dependent manner

In this section, we more closely investigate the relationship between focal adhesion length and fibril morphometrical and mechanical properties and the substrate stiffness. In Fig. S1, we plot the focal adhesion length and the fibril properties as a function of the number of FN molecules, for different values of substrate stiffness k_{sub}. We compute these measures by averaging the given fibril properties over all time points for which the fibril is composed of the specified number of FN molecules (with windows of 10 FN molecules). Interestingly, we observe that the relationship between some properties and the number of FN molecules depends on substrate stiffness, while other properties do not depend on substrate stiffness.

As expected, stretched and relaxed length and focal adhesion length all increased as the number of FN molecules increases. In general, for a fibril comprised of a given number of FN molecules, the stretched length increases as k_{sub} increases, more so for larger FN molecule values (Fig. S1A). In Fig. 7E, we show that the average stretched fibril length increases as a function of a substrate stiffness k_{sub}. By examining the same relationships for the relaxed length and FN extensibility (stretched/relaxed ratio), we can determine to what extent fibril architecture versus fibril elasticity dictate the stretched fibril length for different substrate stiffness. We find that on soft substrates (k_{sub} = 0.1 pN/nm; dark blue), the relaxed length is shorter, for a given number of FN molecules, compared with larger values of k_{sub}, which suggests that the fibril architecture, and not the stretch of individual Type III domains, is playing a larger role in governing stretched fibril length. In contrast, on more rigid substrates, the relationship between relaxed length and the number of FN molecules does not depend on substrate stiffness, meaning that for a given number of FN molecules, fibril architectures are comparable, regardless of substrate stiffness. However, we find that FN extensibility, in general, increases as a function of substrate stiffness, for a given number of FN molecules (Fig. S1C), which, in conjunction with comparable fibril architectures, demonstrates that individual Type III domains are more stretched as substrate stiffness increases. These predictions are also consistent with the overall increase in FN extensibility as a function of substrate stiffness, observed in Fig. 7G.

A thorough analysis of the model predictions can explain the U-shaped dependence of focal adhesion stress, as a function of substrate stiffness, shown in Fig. 6A. For all substrate stiffnesses, the fraction of attached molecular clutches increases as the number of FN molecules increases (Fig. S1D). However, this fraction is larger on soft substrates, in particular for FN molecule values between 0 and approximately 300 molecules. Interestingly, this does not lead to larger substrate forces. Substrate force increases as the number of FN molecules increases; however this relationship is independent of k_{sub} (Fig. S1E).

Significantly, this suggests that on soft substrates, a fibril comprised of a given number of FN molecules on average has more integrin bound connections, compared with more rigid substrates, but still only generates the same substrate force. Following Eq. 5, actin velocity decreases as the number of FN molecules increases, and is similarly independent of k_{sub} (Fig. S1F). As a consequence, focal adhesion length is smaller on softer substrates, compared to more rigid substrates (Fig. S1G). Thus, smaller focal adhesion length in the presence of comparable substrate forces results in a larger focal adhesion stress on soft substrates. On intermediate substrate stiffnesses (k_{sub} = 10 pN/nm; cyan), focal adhesion length is consistently larger for large numbers of FN molecules, reducing the focal adhesion stress, while on more rigid substrates (k_{sub} = 100 and 1000 pN/nm; yellow, orange), focal adhesion length is moderately smaller, such that focal adhesion stress is increased, producing the U-shaped dependence observed for focal adhesion stress as a function of substrate stiffness.

Further analysis can also explain the seemingly contradictory observation that terminal FN fibrils are, on average, longer but comprised of fewer FN molecules, as observed in Fig. 7E and H, on more rigid substrates. First, we note that the probability of fibril assembly termination, shown as a function of the number of FN molecules, does show a dependence on substrate stiffness (Fig. S1H). This probability increases as a function of FN molecule count, for all substrate stiffness, as expected. For fibrils with a small number of FN molecules (less than 300), the probability of assembly termination is U-shaped as a function of substrate stiffness, that is, fibril assembly is more likely to terminate on either a very soft or very rigid substrate, but less likely to terminate on an intermediate substrate stiffness. However, for a fibril comprised of larger number of FN molecules, this trend shifts, such that the probability of assembly termination decreases as k_{sub} decreases. Collectively, these relationships result in the generally negative correlation between substrate stiffness and the number of FN molecules at assembly termination, observed in Fig. 7H. However, the increase in FN extensibility and elasticity of individual Type III domains on more rigid substrates more than compensates for the fewer number of FN molecules, such that the average stretched length increases as a function of substrate stiffness (Fig. 7E).

Mechanotransduction model predictions of unloaded actin velocity dependence

The above analysis demonstrated that the substrate stiffness provides critical feedback during the fibril assembly process that alters FN extensibility, integrin binding, focal adhesion length, and termination of the assembly process itself. In addition to altering the distribution of cell-generated forces, the substrate stiffness provides this feedback through regulation of the actin velocity, which in turn governs the stretching of the fibril. We next investigated the dependence of the unloaded actin velocity v_u on our model, to demonstrate the dependence

of the velocity on fibril properties. Physiologically, actin velocity can range several orders of magnitude, depending on cell type and myosin phosphorylation, with values ranging from 8 to 4600 nm/s in dephosphorylated myosins from platelet cells to fast skeletal muscle myosins, respectively (14). We first investigated our model on a rigid substrate (k_{sub} = 1000 pN/nm). For slow v_u = 10 nm/s, substrate force f_{sub} of the assembled fibrils remains essentially constant, with small fluctuations due to the breaking and creation of integrin bounds (Fig. S2A, black). In contrast, for fast $v_u = 10^4$ nm/s, f_{sub} remains near zero, with frequent large fluctuations due to integrin rupture events (Fig. S2A, green). An intermediate v_u = 300 nm/s produces an intermediate response, with sustained large substrate forces but significant fluctuations due to integrin binding breakage (Fig. S2A, red, c.f. Fig. 7B in the main text). Thus, our model predicts that, on average, substrate forces decrease as the unloaded actin velocity increases (Fig. S2B), and this result does not depend on the substrate stiffness. Similarly, the average fraction of attached molecular clutches also decreases as the unloaded actin velocity increases, independent of substrate stiffness (Fig. S2C). Critically, we find that a fast actin velocity produces dynamics similar to the frictional slippage regime observed in the Chan-Odde model (Fig. 7A), such that frequent integrin rupture events prevent sustained substrate forces necessary for FN-FN binding events. However, in contrast with the Chan-Odde model, this regime does not depend on substrate rigidity, but rather the cell-state dependent property of actin velocity. These findings confirm experimental evidence that either myosin inhibitors or myosin *activators* impair FN fibril assembly (15).

As a consequence, the fibril assembly processes is increasingly truncated as the unloaded actin velocity increases (Fig. S2D-G), such that stretched length, relaxed length, and the number of FN molecules all decrease as a function of v_u. Further, FN extensibility is also decreased, consistent with reduced extensibility in fibrils of fewer FN molecules in Fig. S1C. The prediction that substrate forces are reduced as actin velocity increases seems surprising, when also considering that larger actin velocities are associated with myosins from cells that generate considerable forces, e.g., fast skeletal muscle. However, it is important to note that the model prediction of reduced substrate force is primarily a consequence of greatly reduced fibril assembly, due to frictional slippage dynamics, independent of substrate stiffness. This has been experimentally confirmed through studies that show that large forces on stiff surfaces require FN assembly, and that inhibition of FN assembly impairs force generation (16). Thus, the model predicts that cells with large actin velocity are not ideal to assemble FN fibrils, but further work is needed to predict how actin velocity and substrate stiffness influence substrate forces for fully assembled FN fibrils. This is of great interest and is an area of ongoing investigation.

SUPPORTING FIGURES

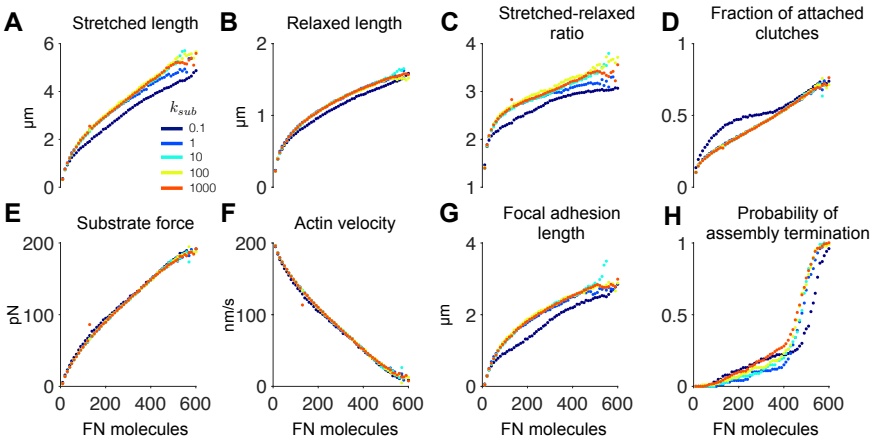

Figure S1: Number of fibronectin molecules predicts fibril morphometrical and mechanical properties in a substrate-dependent manner. (A) Stretched length, (B) relaxed length, (C) fibril extensibility (stretched-relaxed FN length ratio), (D) the fraction of attached molecular clutches, (E) substrate force, (F) actin velocity, (G) focal adhesion length, and (H) the probability of fibril assembly termination are shown as a function of the number of fibronectin (FN) molecules, for different values of substrate stiffness k_{sub}. In panels A-G, each data point is calculated by averaging the given fibril properties over all time points for fibrils composed of the specified number of FN molecules (with windows of 10 FN molecules).

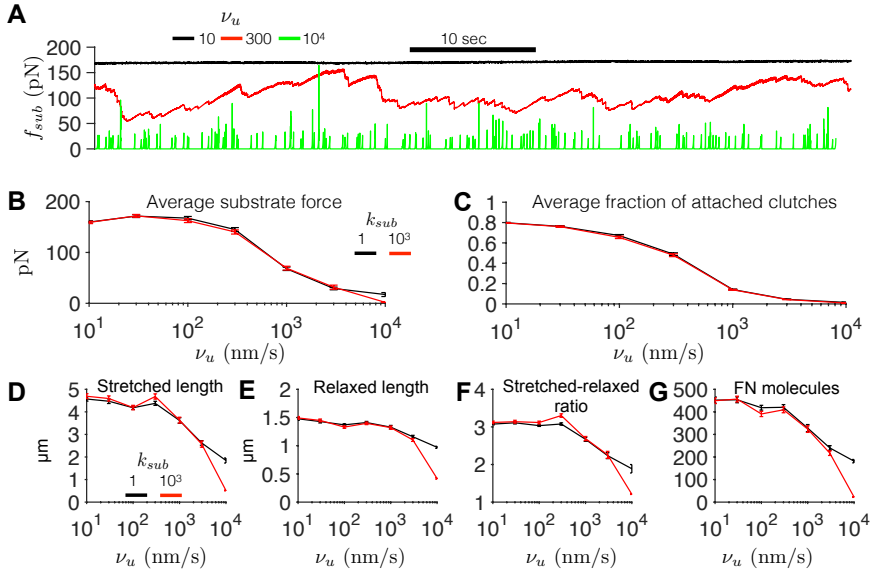

Figure S2: Mechanotransduction model predictions of unloaded actin velocity dependence. (A) Substrate force f_{sub} as a function of time for different unloaded actin velocity values ν_u. Model mean ± standard error, for (B) substrate force and (C) fraction of attached molecular clutches are shown as a function of ν_u for different substrate stiffness values k_{sub}. Mean ± standard error, for (D) stretched length, (E) relaxed length, (F) stretched-relaxed length ratio, and (G) number of FN molecules are shown as a function of ν_u for different substrate stiffness values k_{sub}. In A, $k_{sub} = 1000$ pN/nm. In B-G, model averages are computed by time-averaging over the minute preceding FN assembly termination, and then averaged over 100 simulations.

SUPPORTING TABLES

Table S1: *Molecular clutch, substrate, and actin parameters.*

Parameter	Definition	Units	Value
ν_{on}	Clutch engagement rate	s^{-1}	0.1 (1)
ν_{off}	Unstretched clutch disengagement rate	s^{-1}	0.01 (17)
k_c	Clutch spring constant	pN/nm	5 (1, 18)
f_b	Clutch break force	pN	2 (1, 19)
k_{sub}	Substrate spring constant	pN/nm	0.1-1000
v_u	Unloaded actin velocity	nm/s	200 (14, 20)
f_{stall}	Actin stall force	pN	$N_{myo}f_{myo}$
N_{myo}	Number of myosin motors	-	100 (1)
f_{myo}	Unitary myosin motor force	pN	2 (1, 21)

Table S2: *FNIII domain and fibril parameters.*

Parameter	Definition	Units	Value
$k_{1,0} = k_{30,0}$	FNIII-1 resting stiffness	pN/nm	0.4*
$k_{2,0} = k_{29,0}$	FNIII-2 resting stiffness	pN/nm	0.8*
$k_{3,0} = k_{28,0}$	FNIII-3 resting stiffness	pN/nm	0.3*
$k_{4,0} = k_{27,0}$	FNIII-4 resting stiffness	pN/nm	0.9*
$k_{5,0} = k_{26,0}$	FNIII-5 resting stiffness	pN/nm	1.0*
$k_{6,0} = k_{25,0}$	FNIII-6 resting stiffness	pN/nm	0.6*
$k_{7,0} = k_{24,0}$	FNIII-7 resting stiffness	pN/nm	0.9*
$k_{8,0} = k_{23,0}$	FNIII-8 resting stiffness	pN/nm	0.8*
$k_{9,0} = k_{22,0}$	FNIII-9 resting stiffness	pN/nm	0.7*
$k_{10,0} = k_{21,0}$	FNIII-10 resting stiffness	pN/nm	0.5*
$k_{11,0} = k_{20,0}$	FNIII-11 resting stiffness	pN/nm	0.3*
$k_{12,0} = k_{19,0}$	FNIII-12 resting stiffness	pN/nm	0.6*
$k_{13,0} = k_{18,0}$	FNIII-13 resting stiffness	pN/nm	0.5*
$k_{14,0} = k_{17,0}$	FNIII-14 resting stiffness	pN/nm	0.8*
$k_{15,0} = k_{16,0}$	FNIII-15 resting stiffness	pN/nm	0.7*
k_{max}	Maximum domain stiffness	pN/nm	10^6 (for numerical stability)
τ_ω	Domain stiffness relaxation time constant	s	0.01*
λ_ω	Domain stiffness space constant	nm	1*
χ_d	Domain contour length	nm	30.6 (5)
χ_p	Domain persistence length	nm	0.5 (5)
r	FNIII molecule radius	nm	1 (22)
ϵ_t	Domain binding site exposure threshold	nm	1.5 (23)
η	Domain binding site exposure scaling factor	-	6*
ν_{FN}	Soluble FN binding rate	$\text{nM}^{-1}\ \text{s}^{-1}$	0.001*
$[\mathcal{S}]$	Extracellular soluble FN concentration	nM	20 (24)

* indicates that the parameter value was estimated. See Supporting Methods for details.

SUPPORTING MOVIES

Movie S1: Simulation of fibronectin fibril assembly, shown in Fig. 2 and 4. (Top) The Hookean spring network and position along the z-axis is shown as a function of time. Elastic fibronectin (FN) type III domains (black), FN-FN binding (red), inelastic FN type I and II domains (blue), and integrin binding (green) are shown. (Bottom, left) The FN fibril cross-section in the x-y plane is shown, with FN-FN connections (red). (Bottom, right) The three-dimensional FN fibril architecture is shown. The first hour is shown with 1 minute time increments, and the subsequent 16 hours are shown in 15 minute time increments.

SUPPORTING REFERENCES

[1] Chan, C. E., and D. J. Odde, 2008. Traction Dynamics of Filopodia on Compliant Substrates 322:1687–1691.

[2] Bell, G. I., 1978. Models for the specific adhesion of cells to cells. *Science* 200:618–627.

[3] Ferreira, A. J. M., 2008. MATLAB Codes for Finite Element Analysis, volume 157 of *Solids and Structures*. Springer Science & Business Media, Dordrecht.

[4] Bustamante, C., J. Marko, E. Siggia, and S. Smith, 1994. Entropic elasticity of lambda-phage DNA. *Science* 265:1599–600.

[5] Marko, J. F., and E. D. Siggia, 1995. Stretching DNA. *Macromolecules* 28:8759–8770.

[6] Stirnemann, G., D. Giganti, J. M. Fernandez, and B. Berne, 2013. Elasticity, structure, and relaxation of extended proteins under force. *Proc. Natl. Acad. Sci. U.S.A.* 110:3847–52.

[7] Gillespie, D. T., 1977. Exact stochastic simulation of coupled chemical reactions. *Journal Phys Chem* 81:2340–2361.

[8] Alfonsi, A., E. Cancès, G. Turinici, B. Di Ventura, and W. Huisinga, 2005. Adaptive simulation of hybrid stochastic and deterministic models for biochemical systems. *ESAIM* 14:1–13.

[9] Nivala, M., E. de Lange, R. Rovetti, and Z. Qu, 2012. Computational modeling and numerical methods for spatiotemporal calcium cycling in ventricular myocytes. *Front Physiol* 3:114.

[10] Oberhauser, A. F., B. Carmelu, C. Mariano, and J. M. Fernandez, 2002. The Mechanical Hierarchies of Fibronectin Observed with Single-molecule AFM 319:433–447.

[11] Lemmon, C. A., T. Ohashi, and H. P. Erickson, 2011. Probing the Folded State of Fibronectin Type III Domains in Stretched Fibrils by Measuring Buried Cysteine Accessibility 286:26375–26382.

[12] Mcdonagh, J., 1985. Plasma Fibronectin. Structure and Functions. CRC Press.

[13] Berg, J. M., J. L. Tymoczko, and L. Stryer, 2002. Biochemistry. W. H. Freeman.

[14] Cuda, G., E. Pate, R. Cooke, and J. R. Sellers, 1997. In vitro actin filament sliding velocities produced by mixtures of different types of myosin 72:1767–1779.

[15] Lemmon, C. A., C. S. Chen, and L. H. Romer, 2008. Cell Traction Forces Direct Fibronectin Matrix Assembly 96.

[16] Scott, L. E., D. B. Mair, J. D. Narang, K. Feleke, and C. A. Lemmon, 2015. Fibronectin fibrillogenesis facilitates mechano-dependent cell spreading, force generation, and nuclear size in human embryonic fibroblasts. *Integr Biol (Camb)* 7:1454–65.

[17] Lele, T. P., C. K. Thodeti, J. Pendse, and D. E. Ingber, 2008. Investigating complexity of protein–protein interactions in focal adhesions. *Biochemical and Biophysical Research Communications* 369:929–934.

[18] Fisher, T. E., A. F. Oberhauser, M. Carrion-Vazquez, P. E. Marszalek, and J. M. Fernandez, 1999. The study of protein mechanics with the atomic force microscope. *Trends Biochem. Sci.* 24:379–384.

[19] Jiang, G., G. Giannone, D. R. Critchley, E. Fukumoto, and M. P. Sheetz, 2003. Two-piconewton slip bond between fibronectin and the cytoskeleton depends on talin. *Nature* 424:334–337.

[20] Umemoto, S., A. R. Bengur, and J. R. Sellers, 1989. Effect of multiple phosphorylations of smooth muscle and cytoplasmic myosins on movement in an in vitro motility assay. *Journal of Biological Chemistry* 264:1431–1436.

[21] Molloy, J. E., J. E. Burns, J. Kendrick-Jones, R. T. Tregear, and D. C. White, 1995. Movement and force produced by a single myosin head. *Nature* 378:209–212.

[22] Leahy, D., I. Aukhil, and H. Erickson, 1996. 2.0 A crystal structure of a four-domain segment of human fibronectin encompassing the RGD loop and synergy region. *Cell* 84:155–64.

[23] Gao, M., D. Craig, V. Vogel, and K. Schulten, 2002. Identifying Unfolding Intermediates of FN-III10 by Steered Molecular Dynamics. *Journal of Molecular Biology* 323:939–950.

[24] Ylätupa, S., C. Haglund, P. Mertaniemi, E. Vahtera, and P. Partanen, 1995. Cellular fibronectin in serum and plasma: a potential new tumour marker? 71:578–82.